3. GLOBAL OCEANS–J. M. Levy, Ed.

a. Overview–J. M. Levy

As the global ocean observing system matures and climatologies of essential climate variables grow more robust, observations of anomalous departures continue to shed light on the evolving behavior of the coupled ocean–atmosphere system. The year 2007, while less anomalous than 2006, was characterized by the following key findings:

- Global sea surface temperature during 2007 showed significant departures from the 1971–2000 climatology in four regions: the positive anomaly in the high-latitude North Atlantic that has persisted since 2002 continued into 2007; positive anomalies that have occurred each boreal summer since 2002 in the Arctic Ocean adjacent to the North Pacific reached their highest value of about 2.5°C in 2007; the positive anomaly in the tropical North Atlantic that has been trending downward from its highest value in 2005 returned to near-normal conditions in the summer of 2007; and positive anomalies in the central and eastern equatorial Pacific associated with the 2006 El Niño ended in February 2007, and a moderate-strength La Niña developed in the fall of 2007.
- Annual average upper-ocean heat content anomalies declined between 2006 and 2007 in the eastern equatorial Pacific and increased in off-equatorial bands in that ocean. These changes were consistent with the transition from El Niño in 2006 to La Niña in 2007.
- Ocean heat fluxes demonstrated a coherent pattern of change in the tropical Pacific, in response to the east–west SST pattern of the 2007 La Niña episode. Evaporative heat loss decreased over the cooler SST region in the eastern Pacific and increased over the warmer SST region in the western Pacific. Variations of ocean heat fluxes in the tropical Pacific on ENSO time scales are a dominant interannual signal.
- The tropical cyclone heat potential, a parameter proportional to the upper-ocean heat content that is linked to hurricane intensification, exhibited high variability within each ocean basin. On average, all basins, except the eastern Pacific basin, showed areas of positive values. The west Pacific Ocean had the largest anomaly values of this parameter.
- Global sea surface salinity anomalies in 2007 continued to accentuate climatological patterns; fresh areas of the ocean have generally become fresher and salty areas have generally become saltier in recent years relative to a long-term climatology. These changes suggest a possible increase in the strength of the hydrological cycle.
- Westward surface current anomalies dominated the equatorial Pacific basin, reflecting the La Niña conditions that developed in the second half of 2007. Long-term trends in eddy kinetic energy reveal that major ocean currents such as the Gulf Stream, Kuroshio, Brazil, and Malvinas Currents are shifting in position and/or strength; these decadal-scale changes may reflect longer-term fluctuations or secular trends.
- A new basinwide time series capturing the entire Atlantic meridional overturning circulation at 26.5°N demonstrated that the variability of the MOC is much higher at time scales of weeks to months than had previously been believed. Consistent with observations that Florida Current transport, representing the upper limb of the MOC, was at its climatological mean in 2007, the high degree of observed variability makes it impossible at this time to rule in or out any long-term trend in the MOC.
- The global mean SLA in 2007 was 1.1 mm higher than in 2006, which is about one standard deviation below what would be expected from the 15-yr trend value of 3.4 mm yr^{-1}. However, when combined with the SLA of 6 mm in 2006, the 2-yr increase matches the 15-yr trend. Dominant spatial patterns of sea level variability during 2007 included the strengthening La Niña in the tropical Pacific Ocean, and zonal anomalies in the tropical Indian Ocean, particularly south of the equator.
- A revised global surface pCO_2 climatology, assembled from over 3 million measurements spanning 36 yr, suggests a 30% larger inter-annual variability in ocean CO_2 uptake than that inferred from the previous climatology, which incorporated far fewer observations.
- Chlorophyll concentrations during 2007 were close to the mean value derived from 10 yr of climate-quality ocean color measurements, but exhibited significant climate-related deviations from the mean that were largely due to global changes in phytoplankton physiology rather than phytoplankton biomass.

b. Temperature

1) Sea Surface Temperatures in 2007—R. W. Reynolds and Y. Xue

SSTs have been derived as monthly fields interpolated from the weekly 1° OI analyses of Reynolds et al. (2002) and as daily fields from the daily 1/4° OI

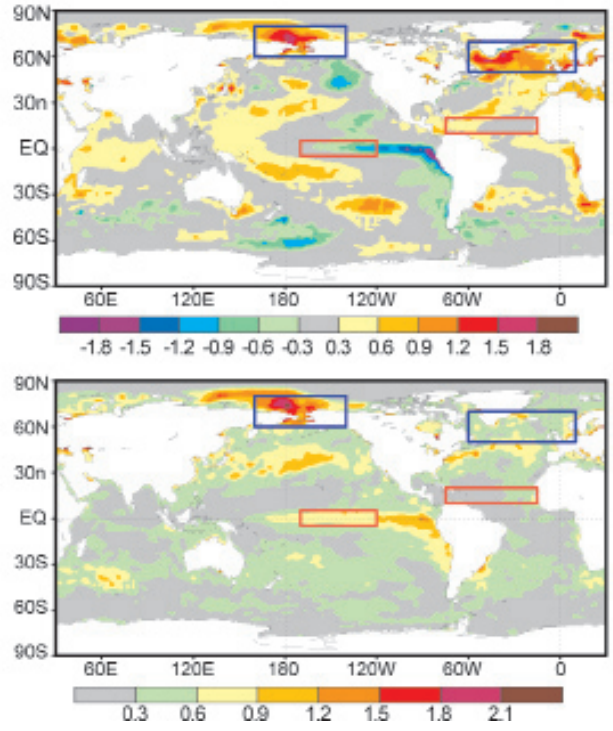

Fig. 3.1. Mean and standard deviation of monthly SST anomalies for 2007 on a 1° spatial grid. The anomalies are computed relative to a 1971–2000 base period. Boxes indicate time-series regions discussed in Fig. 3.2.

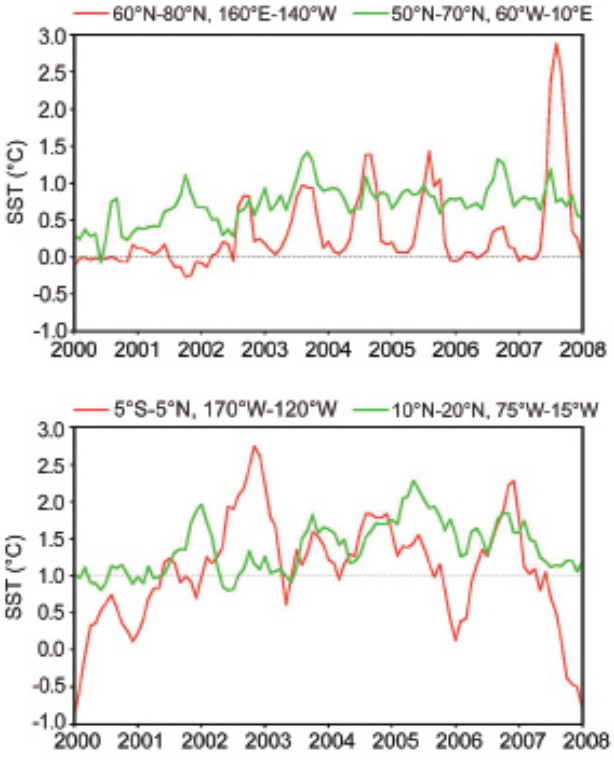

Fig. 3.2. Time series of monthly SST anomalies (top) for two northern high-latitude regions (blue boxes in Fig. 3.1) and (bottom) for two tropical regions (red boxes in Fig. 3.1).

analyses of Reynolds of et al. (2007). Both analyses use ship and buoy in situ SST data as well as satellite SST retrievals. The weekly OI analysis uses satellite retrievals from the IR AVHRR; the daily OI analysis uses satellite retrievals from AVHRR and microwave retrievals from the AMSR. All anomalies are defined as departures from the 1971–2000 climatology described by Xue et al. (2003). Although either analysis is adequate to describe large-scale changes in SST, the daily analysis becomes more useful, on smaller time and space scales.

To illustrate the overall changes in 2007, the yearly average and standard deviation of the monthly anomalies derived from the weekly analysis are shown in Fig. 3.1. As expected, the anomalies are primarily positive due to an overall global warming relative to the climatological base period. There are four important features that are indicated by boxes and shown as time series in Fig. 3.2 for 2000–07. The first feature is due to the strong positive boreal summer anomalies in the North Pacific/Arctic near the Bering Strait. The positive anomalies are mostly due to summer warming that occurred each year beginning in 2002. The summer warming weakened substantially in 2006, but was enhanced in 2007, consistent with the record low summer sea ice coverage. Figure 3.2 shows strong boreal summer anomaly peaks of 1°–1.5°C in 2003–05 and a record maximum above 2.5°C in 2007. The second feature is the strong positive anomaly in the high-latitude North Atlantic, which has persisted since 2001. The strongest Atlantic peak occurred in the summer of 2003 and was associated with high European summer temperatures at that time. The third feature is the tropical North Atlantic positive anomaly that has persisted since mid-2003, although it weakened substantially in 2007. This region is important for summer and fall hurricane formation. Finally, the fourth feature is the El Niño, which peaked in December 2006, terminated dramatically in February, and transitioned into a moderate-strength La Niña by the fall of 2007. The Niño-3.4 region in Fig. 3.2 shows positive anomalies during the second half of 2006 from the El Niño. The positive anomalies transitioned into normal conditions during February 2007. Weak La Niña conditions (Niño-3.4 index < –0.5°C) did not occur until August and continued to strengthen from August through December 2007 into a moderate-to-strong La Niña (see, also, Figs. 3.15 and 3.20). This change is also indicated in the mean

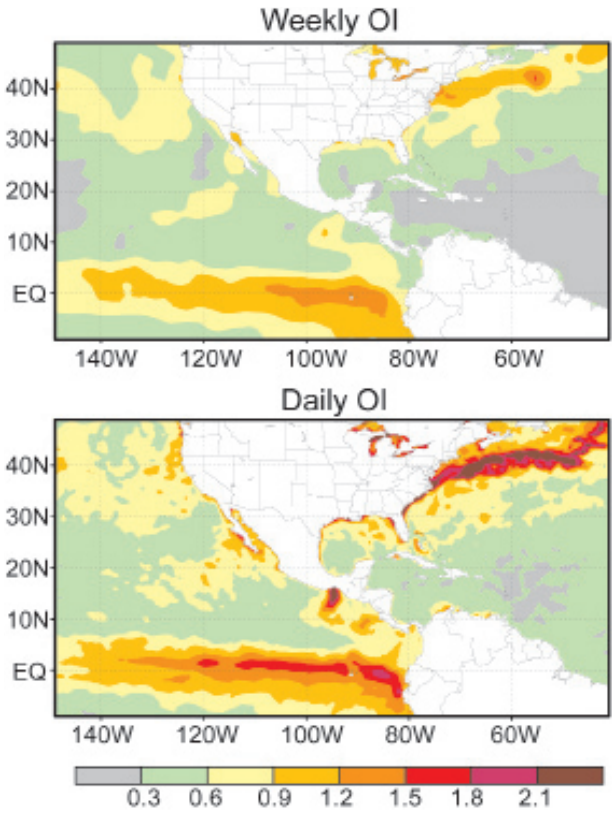

Fig. 3.3. Standard deviation of (top) weekly and (bottom) daily SST anomalies for 2007 on a 1/4° spatial grid. The anomalies are computed relative to a 1971–2000 base period.

by the overall negative anomaly in Fig. 3.1 along the equator in the Pacific and the anomaly standard deviation near 1°C between 120° and 80°W. In addition to these features it is important to point out that a negative Pacific decadal oscillation pattern developed in August 2007 and has persisted into early 2008 (for updated information see http://jisao.washington.edu/pdo/PDO.latest).

Although the large-scale differences between the weekly and daily OI are small, the variability in the daily OI is much larger. This difference can be seen in Fig. 3.3, which shows the daily standard deviation for 2007 for the two analyses. Here the weekly analysis is linearly interpolated in time and space to the day and to the daily analysis grid. The daily OI shows greater variability in the eastern Pacific along the equator and in the Gulf Stream. Compared to the weekly OI, the variability in the Gulf Stream doubles in the daily OI and increases more moderately along the equator in the Pacific. In addition, the daily OI shows greater variability along the coasts and in the Great Lakes. Note in particular, the region of variability in the daily OI off the west coast of Mexico near 15°N. Time series of upwelling off the Oregon coast and in the Niño-1+2 region (10°S–0°, 80°–90°W) show more variability in the daily OI as expected.

To examine one coastal region in more detail, daily and weekly OI time series are shown in Fig. 3.4 off the coast of South Carolina (32°–34°N, 81°–79°W) for 2006 to 2007. This region is chosen to sample the gradients between the Gulf Stream and the coast. These gradients are strongest in the winter when coastal waters are much cooler than the Gulf Stream. The results show that the weekly OI can be up to 5°C warmer than the daily OI during February 2007. The weekly OI has average spatial error correlation scales of 700 km while the daily OI has scales of 100 km. Thus, the difference occurs because the weekly OI is not able to resolve the coastal SST gradients.

2) Ocean Heat Content—G. C. Johnson, J. M. Lyman, and J. K. Willis

Storage and transport of heat in the ocean are central to such aspects of climate as El Niño (e.g., Zebiak 1989), the North Atlantic Oscillation (e.g., Curry and McCartney 2001), hurricane seasons (e.g., Emanuel 2005), and global warming (e.g., Levitus et al. 2005; Hansen et al. 2005).

Here we discuss an estimate of upper (0–750 m) OHCA for the period 1 January–31 December 2007 (Fig. 3.5) analyzed following Willis et al. (2004), but relative to a 1993–2007 baseline. We also discuss changes in OHCA between 2007 and 2006 (Fig. 3.6). In situ ocean temperature data and real-time satellite altimetry are combined using the techniques of Willis et al. (2004) to produce these real-time estimates. In

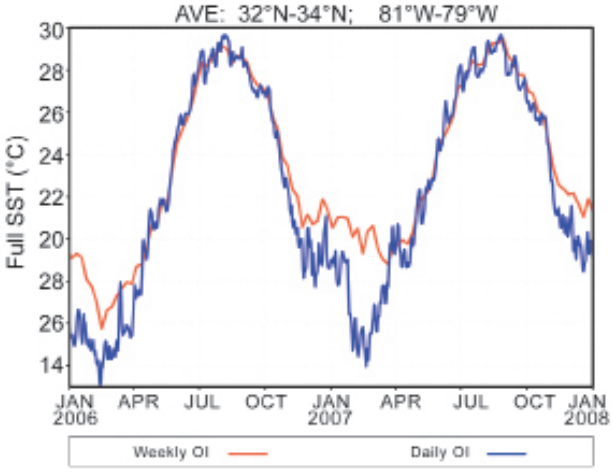

Fig. 3.4. Time series of daily SSTs for the weekly and daily OI analyses for a region just offshore of South Carolina for 1 Jan 2006 through 1 Jan 2008.

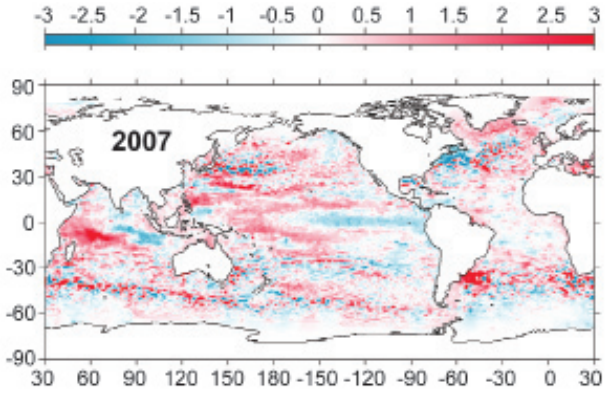

Fig. 3.5. Combined satellite altimeter and in situ ocean temperature data upper (0–750 m) OHCA (10^9 J m^{-2}) map for 2007 analyzed following Willis et al. (2004), but relative to a 1993–2007 baseline.

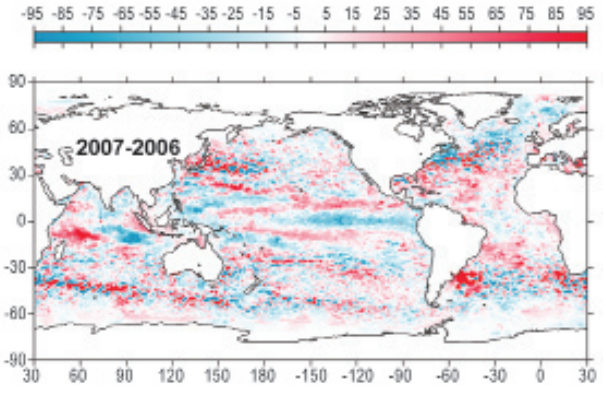

Fig. 3.6. The difference of 2007 and 2006 combined OHCA maps expressed as a local surface heat flux equivalent (W m^{-2}). For purposes of direct comparison with Fig. 3.5, note that 95 W m^{-2} applied over one year would result in 3 ¥ 10^9 J m^{-2} of OHCA.

recent years many of the globally distributed in situ data are from Argo (Roemmich et al. 2004). Data from Argo floats with a recently detected systematic bias in reported pressure values that were not corrected prior to this analysis have been removed from the estimates discussed here. In addition, annual estimates of XBT fall rate corrections have been applied for deep and shallow probe data (e.g., Wijffels et al. 2008). Details of the fields analyzed here may change after data with corrected pressures from the few remaining floats with outstanding pressure-reporting issues are corrected and made available, after more real-time data are subject to delayed-mode scientific quality control, and as XBT fall rate corrections improve.

The 2007 combined OHCA map (Fig. 3.5) shows eddy and meander variability down to the 100-km mapping scales, as does, to a greater extent, the difference of the 2007 and 2006 combined OHCA maps (Fig. 3.6). There is a great deal of small-scale spatial variability in OHCA fields associated with the western boundary currents in every gyre, as well as the Antarctic Circumpolar Current. The difference in combined OHCA maps between 2007 and 2006 (Fig. 3.6) illustrates the large year-to-year variability in ocean heat storage, with changes reaching or exceeding the equivalent of a 95 W m^{-2} magnitude surface flux applied over one year (~3 × 10^9 J m^{-2}). Ocean advection likely plays a significant role in many of these changes. While one would not expect OHCA (Fig. 3.5) and SST (Fig. 3.1) anomalies to be tightly coupled, there are some large-scale visual similarities between the two fields in 2007, even relative to their differing baseline periods.

Large-scale patterns are also evident in OHCA for 2007 (Fig. 3.5) and its difference from 2006 (Fig. 3.6). Along the equatorial Pacific, where there was a band of high heat content in 2006 (Arguez et al. 2007), heat content is below the mean in 2007 east of 180°. In addition to the cooling along the equator in the Pacific (Fig. 3.6), there are bands of cooling along 15°N from the western Pacific to about 180° and reaching from 150°E on the equator to around 90°W and 30°S. The result is that OHCA in these off-equatorial regions, while still above mean values, is much diminished with respect to 2006 values (Arguez et al. 2007). While the annual averaging period presented here is too long for detailed study of the movement of heat associated with the transition from El Niño in 2006 to La Niña in 2007, certainly the change on the equator and perhaps those in the off-equatorial regions as well may be related to those processes (e.g., Zebiak 1989).

The North Atlantic largely warmed south of 40°N and cooled north of 40°N between 2006 and 2007 (Fig. 3.6), suggesting either a southward shift in the subtropical–subpolar gyre boundary or intensification of the North Atlantic Current in 2007 relative to the previous year. This intensification arises because subpolar cooling and subtropical warming increase the dynamic height difference between the gyres, hence strengthening the North Atlantic Current (Curry and McCartney 2001). Despite this subpolar cooling in 2007 relative to 2006, much of the North Atlantic subpolar gyre remains warm in 2007 relative to the baseline period (Fig. 3.5). Although weaker than in 2006, this pattern in 2007 is still consistent with a lower than normal strength of the North Atlantic Current and is probably related to decadal changes in the North Atlantic Oscillation index, including atmospheric forcing of ocean circulation

(Curry and McCartney 2001). This climate index has oscillated during the baseline period, including a relatively high wintertime value in DJFM 2007, but has generally trended toward lower values from 1993 through 2007.

In addition, in 2007 a large and strong cool patch coalesces north of 40°N and west of 55°W in the North Atlantic, as does a warm patch east of the cool one (Fig. 3.5). In the South Atlantic, a warm patch of similar geographical extent centered near 35°S, 50°W develops. Large-scale shifts in the locations or strengths of western boundary current extensions in these basins seem the most likely explanations of these patterns.

In the Indian Ocean the largest changes are centered near 10°S, with cooling in the eastern half of the basin along this parallel, and warming in the western half (Fig. 3.6). These changes cause a warm patch centered near this latitude to shift westward in 2007 (Fig. 3.5) from its position in 2006 (Arguez et al. 2007).

In 2007 (Fig. 3.5), as in 2006 (Arguez et al. 2007), OHCA remains high in the Southern Oceans, in a belt located north of the Antarctic Circumpolar Current. In 2007, from west to east, this high band in OHCA is evident near 40°S south of Africa, trending southward to 55°S south of Tasmania. Similarly, from west to east in the Pacific this ridge in OHCA starts near 40°S east of New Zealand and shifts slowly southward to about 55°S near Drake Passage. Finally, in the Atlantic, there is a region of high OCHA across the basin around 35°S. This change has recently been studied on decadal time scales in the South Pacific (Roemmich et al. 2007) and appears to be related to changes in the wind stress field associated with an increase in the Antarctic Oscillation index. This index reached a peak in 1999, fell into a shallow valley in 2002, and has been near neutral since. It is difficult to discern much large-scale trend in OHCA between 2006 and 2007 in this region (Fig. 3.6), with smaller spatial-scale changes of varying sign predominating in the subpolar regions of the Southern Hemisphere.

3) Global ocean heat fluxes—L. Yu and R. A. Weller

Solar radiation, being the only significant external heat source for Earth, is the primary factor that affects the Earth's climate. Most of the solar energy absorbed by Earth is taken up in the top ocean layer, and the ability of the oceans to store, release, and redistribute the heat ensures that the oceans play a key role in moderating the Earth's climate.

Not all absorbed heat is stored and transported by the oceans; much of the heat is released back to the atmosphere by two heat exchange processes at the air–sea interface: evaporation that releases latent heat and conduction and convection that release sensible heat. These air–sea heat exchanges cool the ocean but warm the air, supplying the heat energy needed to drive the atmospheric circulation and global weather patterns. Clearly, air–sea heat fluxes (i.e., the amount of air–sea heat exchange) are a key measure of the role that the ocean plays in global climate, and their changes on short- and long-term time scales may have important climate implications.

The global LHF+SHF in 2007 and the differences from the year 2006 are shown in Fig. 3.7. The flux estimates were produced by the OAFlux project (Yu and Weller 2007) at WHOI.

The OAFlux products used the state-of-the-art bulk flux algorithm version 3.0 developed from the COARE (Fairall et al. 2003), with input surface meteorological variables from an optimal blending of satellite retrievals (e.g., SSMI, QuikSCAT, AVHRR, TMI, and AMSR-E) and the outputs of surface me-

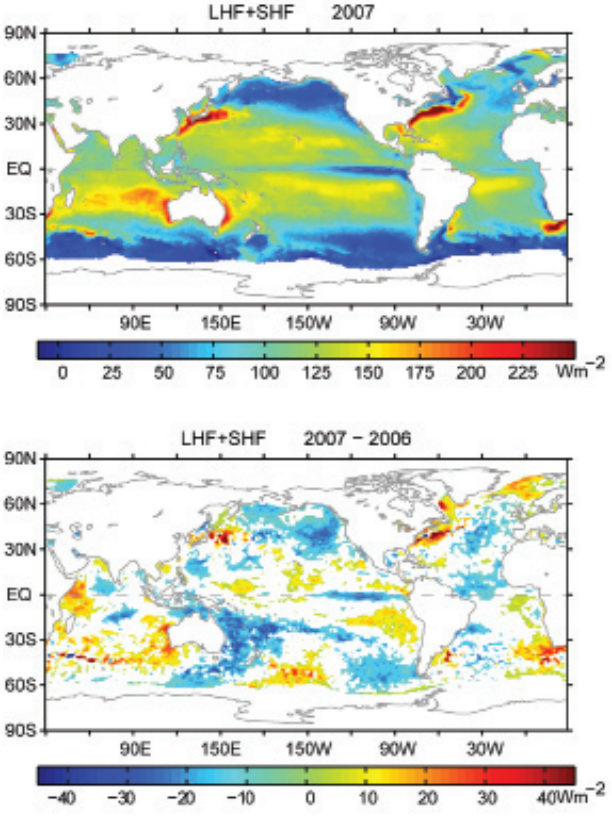

Fig. 3.7. (top) Annual mean latent plus sensible heat fluxes in 2007 (in W m^{-2}). (bottom) Differences between the 2007 and 2006 annual mean latent plus sensible heat fluxes (in W m^{-2}). The sign is defined as upward (downward) positive (negative). The differences significant at the 90% confidence level are plotted.

teorology from reanalysis/forecast models of NCEP and ECMWF (Yu et al. 2008).

The global distribution of latent and sensible heat fluxes is controlled by air–sea temperature/humidity gradients and near-surface atmospheric circulation. On an annual basis, the largest ocean heat losses occur over the regions that are associated with major WBCs and their extensions, the most noted of which are the Kuroshio off Japan, the Gulf Stream off the United States, and the Agulhas Current off the African coast. The magnitude of the annual mean LHF+SHF in these regions exceeds 250 W m^{-2}, produced largely during the fall-to-winter seasons by strong winds and cold and dry air masses coming from the lands. The second largest heat loss (~180 W m^{-2}) is located over the broad subtropical southern Indian Ocean, where the large air–sea heat exchange is sustained primarily by the strong southeast trade winds in the monsoon months June–September.

The LHF+SHF mean difference between 2007 and 2006 shows large-scale, coherent changes over the global basins, with the magnitude of the change within ±50 W m^{-2}. The major change in the tropical oceans is the reduction in LHF+SHF in the central and eastern equatorial Pacific and a slight increase in the western Pacific. This broad east–west contrast is a reflection of the 2007 equatorial Pacific SST structure associated with the La Niña episode of the ENSO cycle. During La Niña, the trade winds in the Pacific Ocean are stronger than normal, driving warm surface waters toward the western Pacific. Meanwhile, the stronger trade winds enhance upwelling of cold deep water near Peru that produces colder than normal SSTs in the eastern basin. As sea surface evaporates more (less) readily over warmer (colder) water, the result is a decrease of latent heat over the colder SST region in the east and an increase of latent heat over the warmer SST region in the west. Variations of ocean heat fluxes in the tropical Pacific on ENSO time scales are a dominant interannual signal in the OAFlux multidecade time series (e.g., Yu and Weller 2007).

The tropical Indian Ocean experienced a short-lived IOD mode event in September–November 2007, which is very unusual during the Pacific La Niña phase. The IOD is characterized by cold SST anomalies off the south Java coast and warm SST anomalies in the western equatorial basin, similar to the La Niña SST pattern in the Pacific. Like the tropical Pacific, the changes in LHF+SHF in the tropical Indian Ocean reflected primarily the changes in SST, and the large increase in LHF+SHF in the western equatorial Indian Ocean is the most notable feature. For the tropical North Atlantic Ocean, the 2007 LHF+SHF was reduced considerably compared to 2006, which was consistent with the regional cooling of SSTs in the two years. The cooling was associated with a persistent high pressure pattern over the Atlantic Ocean, which brought strong northeasterly winds into the tropics that cooled the SSTs through increased upwelling and evaporation. In summary, the close relationship between SST and LHF+SHF in the tropical oceans suggests a response of the atmosphere to the oceanic forcing.

Outside of the tropics, the departure of the 2007 LHF+SHF from 2006 was most pronounced in the vicinity of the WBCs, that is, the Kuroshio, the Gulf Stream, the Agulhas Current, and their extensions. In addition, the increase in LHF+SHF in the northern North Atlantic is worth noting. The enhanced LHF+SHF over the Kuroshio Extension and the Agulhas Current and extension were in phase with the warmer SST difference anomalies (see Fig. 3.1), a further indication of the dominance of the oceanic forcing on the regional air–sea heat exchange. By contrast, the SSTs over the Gulf Stream and its extension were cooler in 2007 than in 2006, as was the case for the SSTs in the northern North Atlantic Ocean. This raises the question of whether SST cooling in the North Atlantic was induced by enhanced evaporative heat loss: In other words, was the change in the Atlantic SST caused by the atmospheric forcing? Further investigation is certainly needed to elucidate the role of air–sea fluxes in the 2007 Atlantic SST variability.

The long-term context of the change in 2007 LHF+SHF is shown in the plot of year-to-year variations of the annual mean averaged over the global oceans from 1958 to 2007 (Fig. 3.8). The 2007 LHF+SHF is at a level similar to the 2006 mean, indicative of insignificant net change. Nevertheless, the two recent years are situated at the high end of a long-term upward trend that started in 1977–78. The upward trend has been driven primarily by LHF, with a minor positive contribution from SHF in the 1990s. Over the past 20 yr from 1978 to 2007, the LHF+SHF has increased by ~ 10 W m^{-2}, from a low at 99 W m^{-2} in 1997 to a high at 109 W m^{-2} in 1999. Since 2000, however, the trend in the time series of the annual mean LHF+SHF has been largely flat.

The oceans, being the source of 86% of the global evaporation and the receiver of 78% of global precipitation, are a key component of the global water cycle. The apparent increase in LHF is consistent with the scenario that evaporation increases as climate warms and hence supports the hypothesized intensification

of the water cycle under global warming. With the availability of continuous satellite-based ocean precipitation records from 1979, a link of evaporation with precipitation records would lead to a better understanding as to how global water cycle has changed in past decades.

4) Tropical Cyclone Heat Potential—G. J. Goni

The role of the ocean in TC formation has been largely recognized and accepted. The formation of Atlantic hurricanes has been linked to the SST, where values of this parameter larger than approximately 26°C have been shown to be a necessary but insufficient condition for hurricane cyclogenesis. Additionally, the intensification of hurricanes involves a combination of favorable atmospheric conditions, such as trough interactions and small vertical shear (DeMaria et al. 1993). After a series of events where the sudden intensification of hurricanes occurred when their path passed over oceanic warm features, it became clear that the upper ocean may play an important role in this process.

Although the sea surface temperature provides a measure of the surface ocean conditions, it gives no information about the subsurface (first tens of meters) ocean thermal structure. It is known that the oceanic skin temperature erodes when the sea surface is affected by strong winds, creating a well-mixed layer that can reach depths of several tens of meters. As the TC progresses, it travels above waters with mixed layer temperatures similar to their skin sea surface temperatures. This provides the motivation to investigate and monitor the upper-ocean thermal structure, which has become a key element in the study of tropical cyclone–ocean interactions focused on prediction of sudden tropical cyclone intensification. Warm ocean features, mainly anticyclonic rings and eddies, are characterized by a deepening of the isotherms toward their centers with a markedly different temperature and salinity structure than the surrounding water mass. We present here results that are used to a) monitor the upper-ocean heat content in all basins where TCs occur, and b) investigate any possible link between this parameter and the growth of intense TCs during 2007.

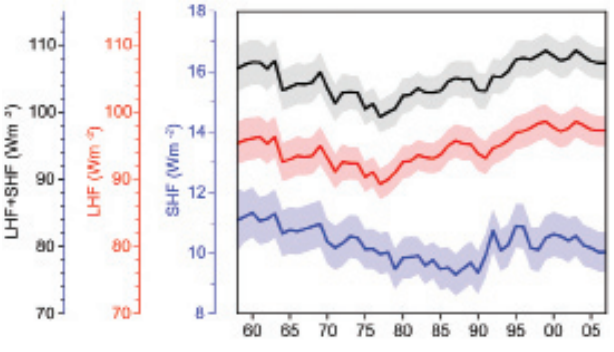

Fig. 3.8. Year-to-year variations of global averaged annual mean latent plus sensible heat flux (upper curve, black), latent heat flux (middle curve, red), and sensible heat flux (bottom curve, blue). The shaded areas indicate the upper and lower limits at the 90% confidence level.

The TCHP is the heat contained in the upper ocean from the sea surface to the depth of the 26°C isotherm. Hydrographic observations cannot provide TCHP fields needed to monitor this parameter on a daily to weekly basis with global coverage. Consequently, a methodology based on a combination of hydrographic and satellite-derived observations is used to create daily global fields of TCHP (Goni et al. 1996; Shay et al. 2000). Statistical analyses of these fields have shown that values of 50 kJ cm^{-2} are usually needed for the ocean to have an effect on the intensification of an Atlantic hurricane (Mainelli et al. 2008). Clearly, areas with high values of TCHP may be important only when TCs travel over them.

There are seven basins where TCs occur: North Atlantic, east Pacific, west Pacific, north Indian, southeast Indian, southwest Indian, and South Pacific. Results presented separate the North Atlantic basin into tropical Atlantic and Gulf of Mexico. The TCHP anomalies are computed during the months of TC activity in each hemisphere: June through November in the Northern Hemisphere and November through April in the Southern Hemisphere. Anomalies are defined as departures from the mean TCHP obtained for the same months from 1993 to 2007. These anomalies show large variability within and among the basins (Fig. 3.9, left).

In the Pacific Ocean, the largest anomalies showed the signature of the negative phase of the 2007 ENSO event (La Niña). However, these anomalies are mostly outside regions where TCs occur, with the exception of the west Pacific and South Pacific basins. The west Pacific showed positive anomalies only, while the South Pacific showed both large positive and negative anomalies. The north Indian Basin exhibited positive values in the Arabian Sea and negative values in the Bay of Bengal. In the mean, the Gulf of Mexico and the tropical Atlantic exhibited small positive anomalies. Nevertheless, within the tropical Atlantic the anomalies were positive (negative) to the south (north) of approximately 25°N. The analysis of the monthly TCHP anomalies averaged over each basin since 1993 (Fig. 3.9) showed that the only two basins

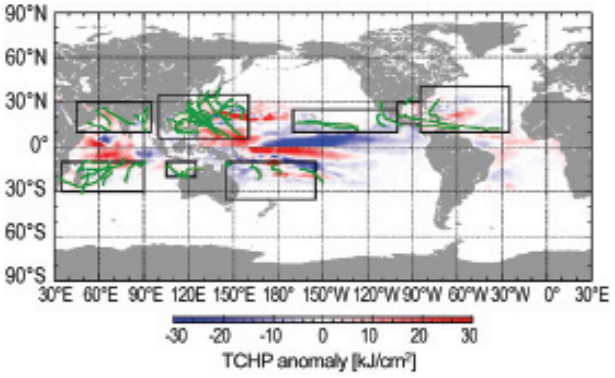

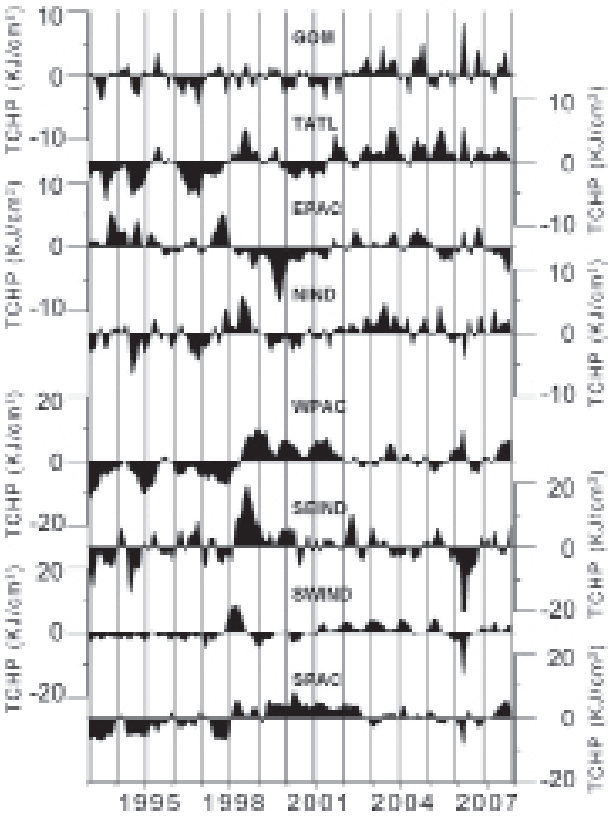

FIG. 3.9. (left) Global anomalies of TCHP corresponding to 2007 computed as described in the text. The boxes indicate the seven regions where TCs occur: from left to right, SWIND, NIND, WPAC, SEIND, SPAC, EPAC, and North Atlantic (shown as GOM and TATL separately). The green lines indicate the trajectories of all tropical cyclones category 1 and above from Nov 2006 to Apr 2007 in the Southern Hemisphere and Jun–Nov 2007 in the Northern Hemisphere. (right) Time series of monthly TCHP anomalies corresponding to each of the seven basins. Note that two different vertical scales are used in this figure.

exhibiting large monthly anomalies (within 75% of their historical extreme values) are the west Pacific and the South Pacific (Fig. 3.9, right). In the mean, all basins, except the eastern Pacific, showed mean positive annual values of TCHP during 2007.

Several TCs were identified to have gained strength when traveling into regions of very high values of TCHP. Some examples of these intensification events are shown in Fig. 3.10. The results presented here correspond to three intense (category 4 and 5) TCs, where the location of their intensification coincided with an increase of the values of TCHP along their tracks. Additionally, the cooling associated with the wake of the TCs is important since it influences the upper-ocean thermal structure on regional time scales within weeks to months after the passage of the cyclones. These TCs were Gonu in the north Indian Basin (Fig. 3.10, top three panels); Krosa in the west Pacific basin (Fig. 3.10, middle three panels); and Felix in the Caribbean Sea (Fig. 3.10, bottom three panels).

(i) Cyclone Gonu

During 3 June to 4 June 2007, cyclone Gonu, a storm with maximum winds of 104 mph (category 2), intensified to maximum sustained winds of 133 mph (category 4). This cyclone intensified when traveling from a region with TCHP value of 60 kJ cm^{-2} over a mesoscale feature with TCHP values averaging 110 kJ cm^{-2}. The average decrease of TCHP and SST under the wake of this cyclone were of 25 kJ cm^{-2} and 3°C, respectively.

(ii) Typhoon Krosa

On 3 October 2007, Typhoon Krosa, a storm with maximum winds of 86 mph (category 1), intensified to one with maximum sustained winds of 138 mph (category 4). This typhoon traveled from a region with TCHP values of 30 kJ cm^{-2} over a mesoscale feature with TCHP values of 75 kJ cm^{-2}. The average decrease of TCHP and SST values under the wake of this typhoon were 50 kJ cm^{-2} and 3°C, respectively.

(iii) Hurricane Felix

On September 2, 2007, hurricane Felix, a cyclone with maximum winds of 104 mph (category 2), intensified to a hurricane with maximum sustained winds of 138 mph (category 4). This hurricane traveled from a region in the Caribbean Sea with TCHP values of 50 kJ cm^{-2} into a region with TCHP values of 110 kJ cm^{-2}. The average decrease of TCHP and SST values under the wake of this hurricane were

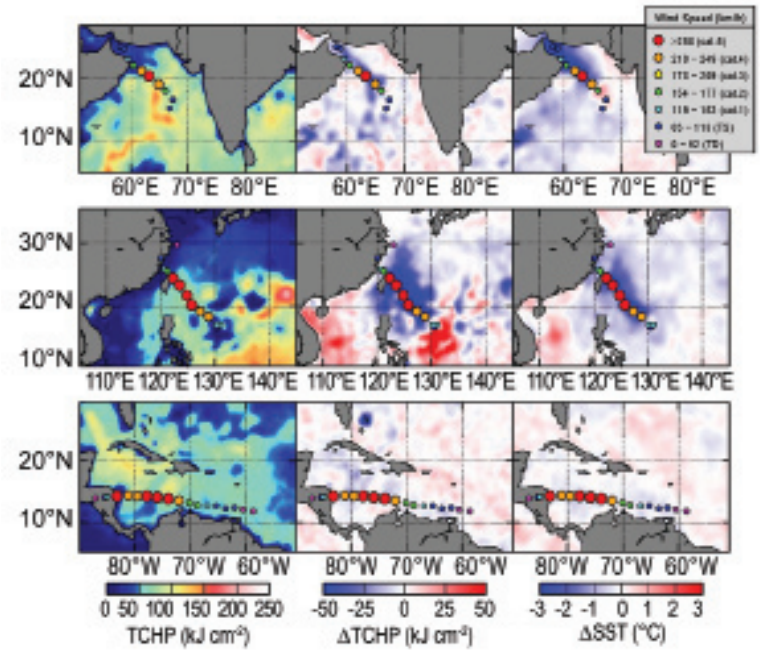

Fig. 3.10. (left) TCHP during three 2007 TCs: (top) Cyclone Gonu, (middle) Typhoon Krosa, and (bottom) Hurricane Felix; (center) TCHP cooling; and (right) SST cooling associated with the wake produced by each TC.

approximately 10 kJ cm^{-2} and 1°C, respectively. The cooling produced by this hurricane is substantially less than that produced by Cyclone Gonu and Typhoon Krosa, probably due to several factors such as translation speed of the storm and vertical ocean stratification.

Altimetry-derived fields of tropical cyclone heat potential provide a measure of the heat contained in warm mesoscale features. The examples presented here show the value of satellite-derived and in situ upper-ocean thermal observations for tropical cyclone intensity studies, suggesting that the inclusion of information on the upper-ocean thermal conditions in air–sea coupled models could help reduce the errors in intensity forecast.

c. Sea surface salinity—G. C. Johnson and J. M. Lyman

Ocean storage and transport of freshwater are intrinsic to many aspects of climate, including the global water cycle (e.g., Wijffels et al. 1992), El Niño (e.g., Maes et al. 2006), and global climate change (e.g., Held and Soden 2006). In the past, in situ ocean salinity data have been too sparse and their reporting too delayed for an annual global perspective of ocean freshwater, and its complement, salinity. However, over the past few years, the now mature Argo array of profiling floats, which measures temperature and salinity year-round in the upper 2 km of the ice-free global ocean (Roemmich et al. 2004), has remedied this situation. The near-global Argo data are analyzed here to determine an annual average SSS anomaly for 2007 relative to a long-term climatology and to describe how annual SSS anomalies have changed in 2007 relative to 2006. Remote sensing of SSS by satellite is planned for 2010 (http://aquarius.nasa.gov/).

In this work the shallowest near-surface (<25 m) salinity data flagged as good from each available Argo profile for 2006 and 2007 were subjected to a statistical check to discard outliers. After this statistical check, the remaining data were then cast as differences from a long-term climatological mean surface salinity field from the *World Ocean Atlas* based on historical data reported through 2001 (*WOA2001*; Boyer et al. 2002). The resulting anomalies were then mapped (Bretherton et al. 1976) assuming a Gaussian covariance function with 6° latitude and longitude decorrelation length scales and a noise-to-signal variance ratio of 2.2. While some delayed-mode scientific controlled (final) Argo data are available for the 2006–07 time period, many real-time (preliminary) Argo data were used in both years. The real-time estimates of SSS made here could change after all the data have been subjected to careful scientific quality control.

SSS patterns are fairly well correlated with surface freshwater flux: the sum of evaporation, precipitation, and river runoff (e.g., Beránger et al. 1999) where advection processes are not dominant. In each ocean basin, subtropical salinity maxima centered between roughly 20° and 25° in latitude are signatures of the predominance of evaporation over precipitation. Conversely, in most regions where long-term climatological surface salinities are relatively fresh, precipitation generally dominates over evaporation. The 2007 anomalies from *WOA2001* (Fig. 3.11) reveal some large-scale patterns. In 2007 the regions around the climatological salinity maxima are mostly salty with respect to *WOA2001*, as they were in 2006 (Arguez et al. 2007) and 2005 (not shown). In many of the climatologically fresh regions, 2007 values appear fresher than *WOA2001*, including: most of the ACC near 50°S, the subpolar gyre of the North Pacific, much of the ITCZ over the Atlantic and Pacific Oceans, and the South Pacific convergence zone west of about 165°W.

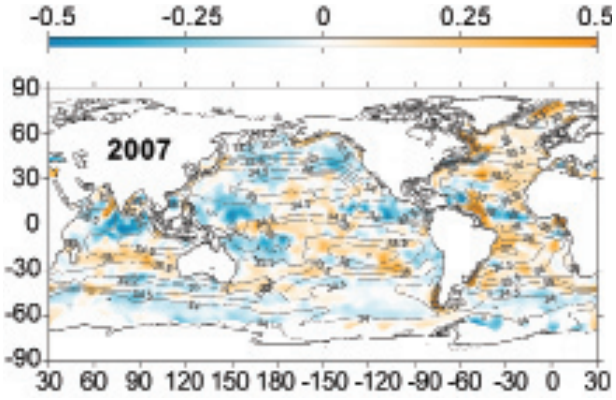

Fig. 3.11. Map of the 2007 annual surface salinity anomaly estimated from Argo data (colors in PSS-78) with respect to a climatological salinity field from *WOA2001* (gray contours at 0.5 PSS-78 intervals). White areas are either neutral with respect to salinity anomaly or are too data-poor to map. While salinity is often reported in psu, it is actually a dimensionless quantity reported on the PSS-78.

These patterns may suggest an increase in the hydrological cycle (i.e., more evaporation in drier locations and more precipitation in rainy areas), as suggested by recent increases in the global ocean average of latent heat flux (Fig. 3.8) and as seen in simulations of global warming. These simulations suggest this signal might be discernible over the last two decades of the twentieth century (Held and Soden 2006). Any increase in the hydrological cycle would certainly result in changes of local SSS values, but not necessarily alter the global average salinity by itself. Most of the anomaly patterns with respect to climatology observed in 2007 (Fig. 3.11) are not reflected in the 2007–2006 differences (Fig. 3.12). Hence, the anomalies observed in 2007 are similar to those observed in 2006 (Arguez et al. 2007) and 2005 (not shown), suggesting that these anomalies have evolved over longer time scales than interannual.

There may be alternate explanations. It is possible that the climatology, being based on relatively sparse data distributions in many parts of the oceans, may tend to underestimate regional extrema that the well-sampled Argo array can better resolve, or that the climatology contains regional biases on seasonal or longer time scales that are not present in the Argo data. Also, some of these patterns might be explained by interannual shifts in ocean features such as the ACC or atmospheric features such as the ITCZ. Indeed, the increase in salinity in the Pacific ITCZ between 2006 and 2007 (Fig. 3.12) is an obvious exception to any claim of long time-scale freshening in that region. Finally, since near-global coverage only commenced around 2005, it is difficult to determine variations on time scales beyond interannual.

Other interesting deviations from high-latitude fresh anomalies are obvious in the relatively salty subpolar North Atlantic and Nordic Seas in 2007 (Fig. 3.11), as well as in 2006 (Arguez et al. 2007), and 2005 (not shown). Year-to-year changes in these regions are relatively small, except in the high lateral gradient areas near the western boundary (Fig. 3.12). This salty subpolar anomaly is inconsistent with an increase in the strength of the hydrological cycle, because with such an increase, one might expect the fresh high latitudes to become fresher. However, the pattern may have less to do with local evaporation and precipitation fields and more with northward spread of saltier waters from the south. The salty anomaly in this region is consistent with a stronger influence of subtropical gyre waters in the northeastern North Atlantic in recent years and a reduced extent for the subpolar gyre (Hátún et al. 2005).

In the Indian Ocean, overall freshening north of about 10°S (Fig. 3.12) has enlarged and intensified the fresh anomaly located south of India around the equator in 2007 (Fig. 3.11) relative to its size and strength in 2006 (Arguez et al. 2007). This anomaly was not present in 2005 (not shown), suggesting an interannual time scale for this feature.

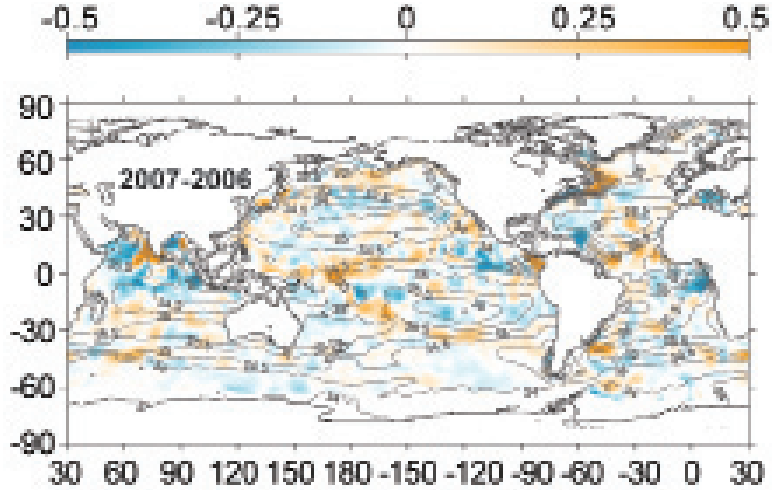

Fig. 3.12. The difference of 2007 and 2006 surface salinity maps estimated from Argo data (colors in PSS-78 yr^{-1} to allow direct comparison with Fig. 3.11). Other details follow Fig. 3.11.

One last feature of interest in the 2007 salinity field is the anomalously salty water located in the region of the fresh Amazon River plume (Fig. 3.11). The influence of this plume would normally be apparent in relatively fresh conditions to the north and west of the mouth of the Amazon River (the cluster of gray contours near 5°N, 40°W) that reach as far north as Puerto Rico. A salty anomaly observed in this region in 2006, but not 2005 (Arguez et al. 2007), intensified east of 60°W in 2007 (Figs. 3.11 and 3.12). This building salty anomaly may be partly explained by reduced freshwater flow from the Amazon into the ocean during a record drought in the Amazon River basin in 2005 (Shein et al. 2006) that continued, although somewhat moderated into 2006 (Arguez et al. 2007), when some time delay for hydrological and oceanic processes is included.

d. Circulation

1) Surface current observations—R. Lumpkin and G. J. Goni

Global analysis of surface currents indicate that westward current anomalies dominated the equatorial Pacific basin, reflecting the La Niña conditions that developed in the second half of 2007. Long-term trends in eddy kinetic energy reveal that major ocean currents such as the Gulf Stream, Kuroshio, Brazil, and Malvinas Currents are shifting in position and/or strength; these decadal-scale changes may reflect longer-term fluctuations or secular trends.

(i) Data and analysis

Near-surface currents are measured in situ by satellite-tracked drifting buoys and by current meters on ATLAS moorings.[1] During 2007, the drifter array ranged in size from a minimum of 1,180 to a maximum of 1,306, with a median size of 1,253 buoys. The moored array consisted of 41 buoys, all but two between 10°S and 21°N. The tropical moored array in the Indian Ocean was expanded considerably in 2007, with several buoys added along 90°E and a new site at 8°S, 67°E. In the Atlantic, the PIRATA array was expanded and now includes moored current meters at four sites along 23°W. The two nontropical moorings in the observing system are at the Kuroshio Extension Observatory (32°N, 145°E) and Ocean Station Papa (50°N, 145°W) sites.

The findings presented here are based on a combined evaluation of mooring, drifter, and satellite-based surface current measurements. Weekly maps of absolute surface currents and geostrophic current anomalies for 2007 were calculated from a synthesis of in situ observations, near-real-time AVISO gridded altimetry, and NCEP operational winds (Niiler et al. 2003). Anomalies are defined with respect to the January 1993–December 1998 mean. Global analyses using similar methodologies (Bonjean and Lagerloef 2002) and validation of surface currents (Johnson et al. 2007) can be found at www.oscar.noaa.gov and www.aoml.noaa.gov/phod/currents.

(ii) Global overview

In 2007, the most dramatic surface current anomalies were westward anomalies spanning the tropical Pacific basin (Fig. 3.13). Maximum annual averaged westward anomalies of 20–25 cm s^{-1} were observed at 120°–125°W on the equator, with annual-averaged values of 5–10 cm s^{-1} elsewhere. As discussed below, these anomalies were strongest during January–March, but were also sustained from mid-July through the end of 2007. These westward anomalies were associated with the La Niña that developed in the latter half of 2007. Anomalies elsewhere in the World Ocean were caused by energetic mesoscale (60–90 day period) variations or were associated with displacements of currents from their typical positions.

Longer-term trends in EKE were obtained from altimetry-derived sea height anomaly observations, to resolve changes in intensity and location of surface geostrophic currents. These trends were calculated for the observations binned in 1° boxes, calculated over the time period 1993–2007. The global observations indicate that large changes in EKE are occurring in all ocean basins, mainly in the most intense surface currents (Fig. 3.14).

(iii) Pacific Ocean

In January–February 2007, westward surface current anomalies developed and intensified across the central equatorial Pacific. During these months, the westward NEC was stronger by 10–30 cm s^{-1} across the basin, while the eastward NECC was barely present. The westward anomalies disappeared from the equatorial Pacific by the end of March 2007.

[1] Drifter data are distributed by NOAA/AOML (www.aoml.noaa.gov/phod/dac/gdp.html). Moored data are distributed by NOAA/PMEL (www.pmel.noaa.gov/tao). Altimetric time series of transports may be viewed online (www.aoml.noaa.gov/phod/satprod). NCEP data provided by the NOAA–CIRES Climate Diagnostics Center (www.cdc.noaa.gov/). AVISO altimetry produced by the CLS Space Oceanography Division as part of the Environmental and Climate EU ENACT project and with support of CNES.

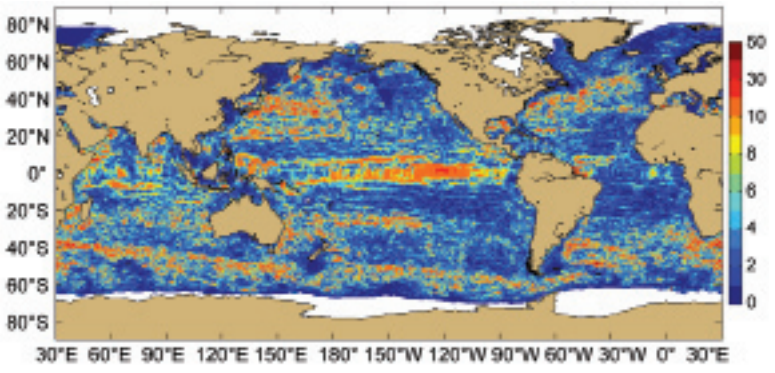

Fig. 3.13. Amplitude (cm s^{-1}) of 2007 annual averaged surface geostrophic current anomalies.

Weak eastward anomalies began developing during March, centered at around 130°W, intensified during April, and were very strong by early May at 110°–160°W. During May 2007, the center of the eastward anomalies shifted to 120°–150°W. Strong off-equatorial (3°–8°N) westward anomalies developed at 130°–180°W. The equatorial eastward anomalies weakened through June.

In July, strong westward anomalies developed in the eastern side of the equatorial Pacific basin (90°–140°W), a pattern that would grow through the remainder of the year to reflect the development of La Niña conditions. Also in July, eastward anomalies developed in the western side of the basin. These patterns created an anomalous confluence along the equator at 150°–160°W. During this period, cold SST anomalies that had previously been confined to the eastern side of the basin began to appear in the Niño-3.4 index region (120°–170°W) (see also, Figs. 3.2 and 3.20).

Through August, the eastward anomalies diminished, then disappeared. The westward anomalies persisted through this month, and intensified in September to expand and span the basin (Fig. 3.15). Also during this month, the Niño-4 index (150°W–160°E) exhibited a sharp drop in surface temperature partly attributable to westward advection of SST anomalies. The basin-scale pattern of westward equatorial anomalies weakened through October, but persisted in a weakened state through November and December 2007.

The long-term trends in EKE reveal large, positive values in the Kuroshio and Kuroshio Extension region (Fig. 3.14), extending to approximately 170°W, which may be related to the regional intensification of surface currents. Baroclinic instabilities of the Kuroshio are the main source of this EKE (cf. Niiler et al. 2003).

(iv) Indian Ocean

During January 2007, the equatorial Indian Ocean exhibited a band of anomalously eastward flow on the eastern half of the basin. Through February, westward anomalies developed in the western half of the basin, and persisted through early March. By April, and persisting through early May, eastward anomalies associated with the equatorial jet were well developed across the equatorial Indian Ocean Basin. This seasonal (monsoon driven) pattern disappeared in May, and in June through September there were no significant current anomalies. In October through November, strong eastward anomalies (the semiannual equatorial jet) developed and propagated across the basin; eastward anomalies persisted in the western third of the basin through December 2007.

The long-term EKE activity in the Agulhas Current region off South Africa (Fig. 3.14) may indicate increasing ring activity. The Agulhas becomes unstable as it separates off the southern tip of South Africa, shedding rings that transport Indian Ocean water into the South Atlantic. This exchange is a significant part of the upper limb of the global meridional overturning circulation, and a decadal-scale increase in this exchange rate may have profound climate implications if verified.

(v) Atlantic Ocean

The seasonal reversal of western tropical Atlantic Ocean currents (cf. Lumpkin and Garzoli 2005) was prominent in 2007. Anomalously strong eastward anomalies were seen on the equator in mid-March through

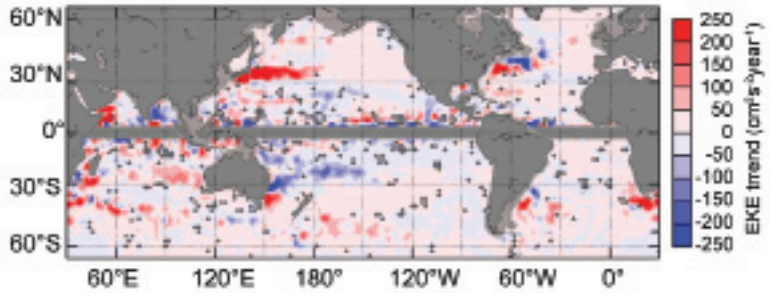

Fig. 3.14. EKE trend, 1993–2007. Crosses show regions where the confidence levels are <67%.

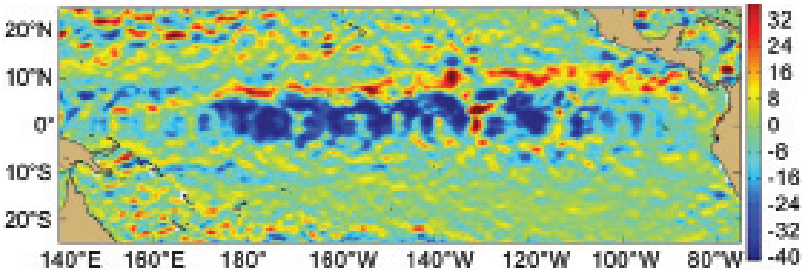

Fig. 3.15. Zonal geostrophic current anomalies (cm s^{-1}) in mid-Sep 2007 in the tropical Pacific, demonstrating the negative (westward) anomalies associated with the development of the 2007 La Niña.

early May. By late May, strong westward anomalies had developed at ~23°W on the equator. These were weak by mid-June, then reintensified in late June through early July, and diminished until they were gone by early August. In September, eastward anomalies were persistent across the central and eastern equatorial Atlantic. This pattern was confined to the Gulf of Guinea by mid-October, and gone entirely by mid-November. Currents in December 2007 were close to their climatological values.

The alternation of positive and negative values in the long-term EKE trend in the northwest North Atlantic and southwest South Atlantic (Fig. 3.14) are indicative of the variability in the subtropical gyres. This change in the South Atlantic is consistent with a shift to the south of the Brazil Current jet (Fig. 3.16). The Brazil Current runs south along the coast until it collides head-on with the northward Malvinas Current; both subsequently turn eastward. During the last 15 yr, the location where the Brazil Current separates from the continental shelf break has moved 2° to the south, possibly indicating an expansion of the South Atlantic wind-driven subtropical gyre (Goni et al. 2008).

2) The meridional overturning circulation—M.O.Baringer and C.S. Meinen

The global ocean–atmosphere system can be thought of as a massive heat engine, redistributing heat from the sun and in so doing causing both short-term weather systems and long-term changes in climate. In the ocean, the so-called MOC is largely responsible for the redistribution of heat, mass and freshwater within the global ocean system. Specifically, the MOC is defined here as the maximum of the zonal integral of mass transport of the large-scale, low-frequency, full-depth ocean circulation. The strengths of the overturning circulations in different basins are directly related to the strength of the heat transport (see Baringer and Meinen 2007 for more discussion). There are several available estimates of the steady-state global mass and heat transport based on inverse model calculations (Lumpkin and Speer 2007; Ganachaud and Wunsch 2003; Talley 2003). Recently, there have been only a few attempts to look at long-term changes in the MOC from direct observations. Bryden et al. (2005) postulate a 30% reduction in the MOC transport between the 1950s and the present day; however, that analysis is based on a very limited dataset (essentially five "snapshot" hydrographic sections). Other recent work using cross-basin hydrographic sections along 48°N in the Atlantic suggest conflicting conclusions relative to the state of the thermohaline circulation. In particular Koltermann et al. (1999) show large variability of the MOC that, they conclude, is related to the strength of Labrador Sea Water production, with larger (smaller) MOC transport corresponding to less (more) Labrador Sea Water export. More recently these data have been reanalyzed to formally test the hypothesis that the MOC circulation is steady. Lumpkin et al. (2008) find that a steady MOC over the same time period could not be ruled out based on the uncertainty in determining the barotropic circulation. It is also noteworthy that the Bryden et al. (2005) suggestion that the thermohaline circulation has declined by 30% over the past 50 yr represents a much higher rate of change than predicted in coupled climate model simulations (e.g., Schmittner

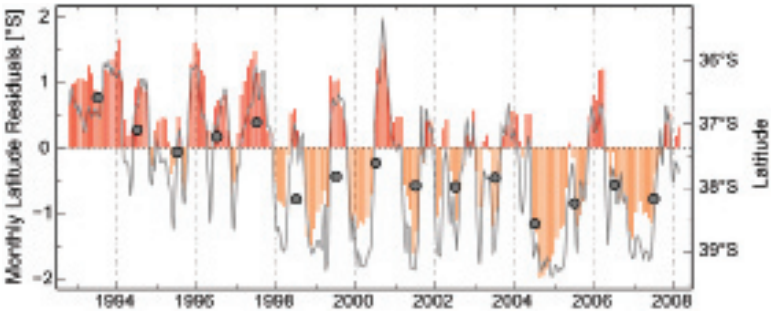

Fig. 3.16. Latitude of separation of the Brazil Current from the continental shelf (black line), monthly anomalies of the separation (vertical bars), and mean annual values (circles) calculated from AVISO altimetry, showing a mean shift to the south of approximately 2°. (From Goni et al. 2008.)

et al. 2005). Clearly, additional work needs to be done to understand the full range of time scales associated with MOC variability and the improvement of error estimates attached to these estimates.

Currently, observing systems capable of quantifying changes in the complete MOC are at fledgling stages that at best observe only one component (e.g., a specific current or ocean layer) of the MOC at discrete locations. At 27°N in the Atlantic the bulk of the warm upper limb of the MOC is thought to be carried in the Florida Current through the Straits of Florida, while the majority of the cold lower limb is believe to be carried to the south in the DWBC just east of the Bahamas. Since 1982, variations in the upper limb of the MOC have been monitored by measuring the Florida Current transport using a submarine cable across the Straits of Florida in combination with regular hydrographic sections. In 1984, monitoring was expanded to the deep limb of the MOC through regular hydrographic cruises (more than 30 to date) across the DWBC east of the Bahamas, and in 2004 the program commenced time series monitoring of the DWBC by adding moored inverted echo sounders and bottom pressure gauges east of Abaco Island in the Bahamas. In 2004 scientists at NOAA joined with collaborators from the University of Miami and the National Oceanography Centre, Southampton, to expand the MOC monitoring array to span the entire Atlantic basin at 26°N using a variety of measurement systems. Called the RAPID Climate Change Program by the U.K. contributors and the MOCHA by the U.S. contributors, this expanded project seeks to develop a cost-effective basinwide MOC monitoring system that will lead to a much greater degree of certainty in the magnitude of the variations in the integrated, basinwide MOC circulations and the time scales on which they vary. Results from the first year of this new MOC monitoring array appeared in *Science* in August (Kanzow et al. 2007; Cunningham et al. 2007). The results from the first year of this array indicate a surprising amount of variability in the MOC strength. In fact, all the MOC values estimated from Bryden et al. (2005) can be found within the first year of the time series (Fig. 3.17). These results cannot disprove the presence of a long-term trend in the strength of the MOC, but they do suggest that a careful error analysis be performed that includes the underlying variability of the MOC (the standard deviation of this first year was estimated as 3.1 Sv).[2]

More recent observations of the strength of the MOC array are available only with a delay in time as the moorings are recovered over 12- to 18-month intervals. However, as noted earlier, the Florida Current contains most of the upper limb of the MOC as it flows through the Straits of Florida in the North Atlantic at 26°N, with a smaller contribution being carried by the Antilles Current east of the Bahamas. Fluctuations in the Florida Current show a clear negative correlation with NAO during the 1982–98 time period (Baringer and Larsen 2001); however, while the NAO has been tending to decrease over the past 20 yr, the Florida Current transport shows no corresponding long-term trend through 2007. The annual mean Florida Current transport observed in 2007 (31.8 Sv) falls only slightly below the long-term mean of 32.1 Sv, and given the statistical standard error of the mean of 1 Sv for a year, 2007 cannot be termed as an unusual year in terms of the Florida Current transport. Compared to 2006 (annual mean of 31.3 Sv) the Florida Current appears to have increased only slightly. Note that 2007 shows similar variability to previous years and no anomalous events occurred during the year (Fig. 3.18).

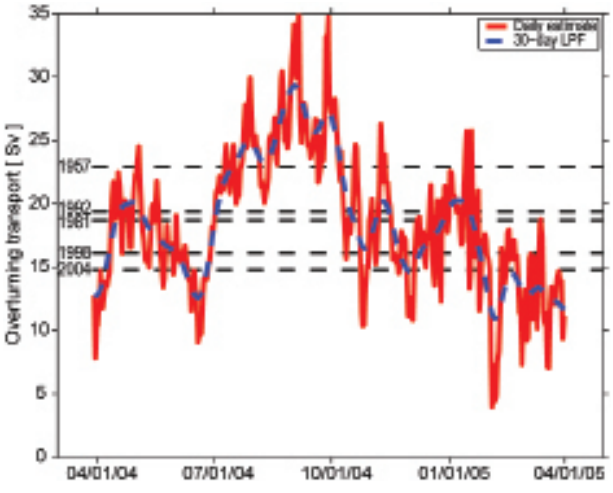

Fig. 3.17. Daily estimates of the strength of the meridional overturning circulation (red solid) as measured by the U.K. NERC Rapid Climate Change Program, the National Science Foundation's MOCHA, and the long-term NOAA Western Boundary Time Series Program. The MOC estimate is based on the upper-ocean transport from 29 Mar 2004 to 31 Mar 2005 based on the interior ocean transport array (adapted from Fig. 3 from Cunningham et al. 2007). The dashed blue line is the 30-day low-pass filtered version of the daily transport values. Dashed black horizontal lines are the Bryden et al. (2005) MOC values from the 1957, 1981, 1992, 1998, and 2004 trans-Atlantic hydrographic sections.

[2] Sverdrup is a unit commonly used for ocean volume transports and is defined as 1 Sv = 10^6 m^3 s^{-1}.

The programs in place since 2004 are an excellent first step toward the development of an integrated MOC measurement system, however, much work remains to fully monitor the Atlantic MOC and the global overturning circulation system. Recent work by Baehr et al. (2008) has shown that an array such as the one deployed at 26°N in the Atlantic may require up to 30 yr of data before a statistically meaningful change in the MOC can be detected.

e. Sealevelvariations—M.A.Merrifield,S.Gill,G.T.Mitchum, and P. L. Woodworth

Global sea level variability during 2007 is summarized using SLA data from the multimission, 1/4° gridded satellite altimeter Aviso product (www.aviso.oceanobs.com/), and RSL from tide gauges primarily from GLOSS (www.gloss-sealevel.org/). SLA and RSL are deviations from a 1993–99 baseline average. The inverse barometer correction has been applied to the SLA, but not to the RSL. We caution that quality controlled delayed-mode SLA data are available only for the first half of 2007 at this time and near-real-time data are used for the second half of the year.[3]

Annual mean SLA in 2007 was above the baseline average for over 80% of the sampled ocean surface (Fig. 3.19a). There is a strong correspondence between mean SLA and RSL patterns. The largest positive deviations occurred in the western equatorial Pacific, the western Indian Ocean, and the Baltic Sea. The region between 20° and 40°S in all oceans was generally above average in sea level. Areas of notable negative sea level deviation include the eastern equatorial Pacific and the northeast Pacific. Relative to 2006 (Fig. 3.19b), areas of increasing sea level include the zonal band just south of the equator in the western Indian Ocean, zonal bands in the general area of the Pacific tropical convergence zones, and the Baltic Sea. Areas of decreasing sea level include the equatorial Pacific cold tongue and the eastern Indian Ocean near 10°S.

The global mean SLA for 2007 was 1.1 mm higher than 2006, as compared to 2006 being 6 mm higher than 2005 (Merrifield et al. 2007). We note that the expected increase of 3 mm in a year has an uncertainty (1 sigma) of about 2 mm for a difference of annual mean values, which indicates that these values of 1 or 6 mm for the annual mean differences are not statistically unlikely. Recent studies have noted the significant increase of the 3.4 mm yr^{-1} trend determined from the 15 yr SLA record compared to the twentieth century consensus estimate of 1.7 mm yr^{-1} obtained using various analyses of the tide gauge dataset (see Bindoff et al. 2007 for a review). An area of active research is the impact of decadal and longer time-scale variations of sea level on global trend estimates. Over the overlap period of satellite altimeters and tide gauges, estimates of global sea level rise from both observing systems are similar (Church et al. 2004; Church and White 2006; Holgate 2007).

Maps of monthly SLA (Fig. 3.20) illustrate the evolving sea level variations that resulted in the annual mean patterns for 2007 (Fig. 3.19a). We begin in September 2006 to illustrate the transition from El Niño to La Niña conditions in the Pacific Ocean. A downwelling Kelvin wave (positive SLA) traveled eastward across the basin during October–December 2006. This was followed by the onset of La Niña conditions with a negative SLA starting in the central equatorial Pacific in January 2007 followed by negative SLA in the cold tongue region beginning in February 2007, and positive anomalies in the western equatorial Pacific and along zonal bands north and south of the equator. The La Niña pattern dominated

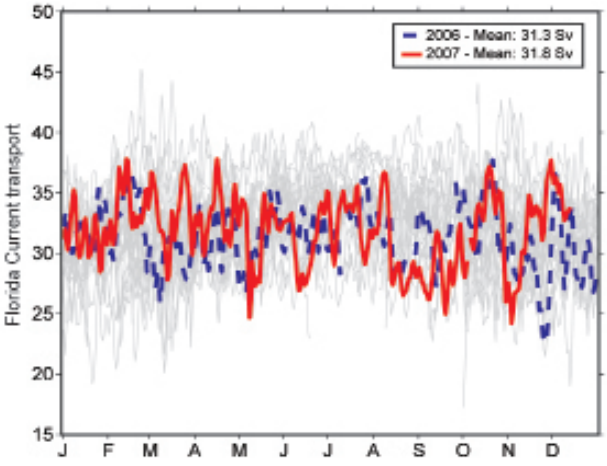

Fig. 3.18. Daily estimates of the transport of the Florida Current for 2007 (red solid line) compared to 2006 (dashed blue line). The daily values of the Florida Current transport since 1982 are shown in light gray. The transport in 2007 increased slightly relative to 2006, but remains slightly below the long-term mean for the Florida Current (32.1 Sv).

[3] The altimeter products were produced by Ssalto/Duacs and distributed by Aviso, with support from CNES (www.aviso.oceanobs.com). The Aviso dataset used is listed as the gridded sea level anomalies DT-MSLA "Ref," multimission product. Tide gauge data were obtained from the University of Hawaii Sea Level Center (http://uhslc.soest.hawaii.edu/). SLA is corrected for atmospheric pressure; the RSL time series are not.

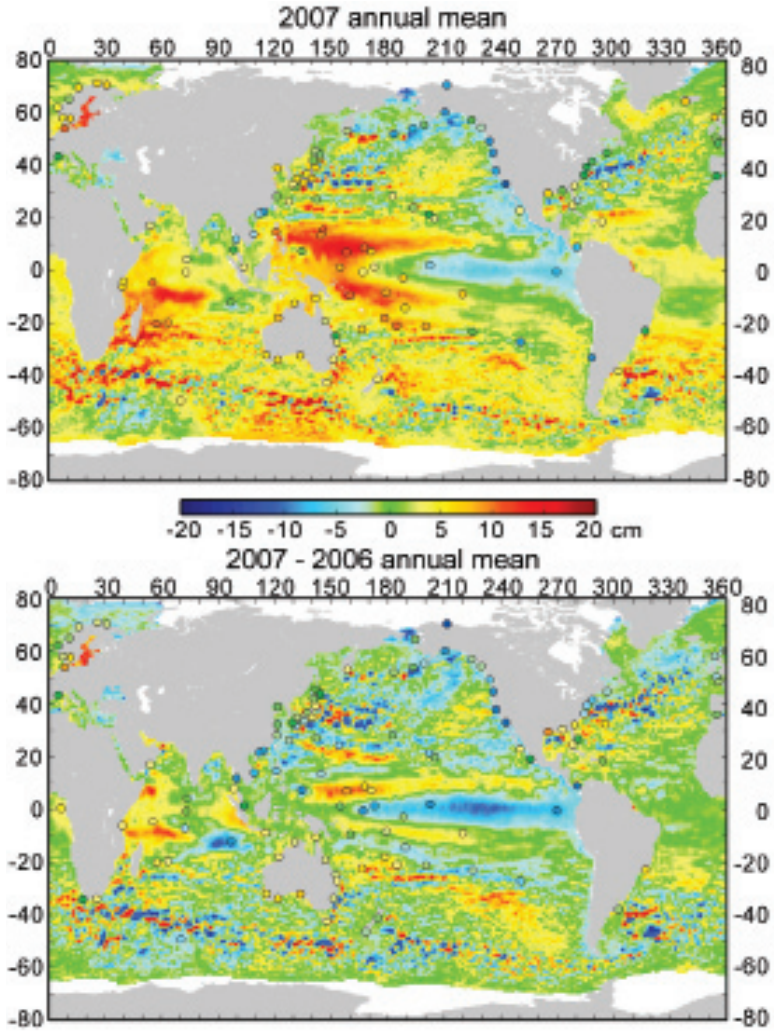

Fig. 3.19. (a) Annual mean (Jan–Dec 2007) SLA and RSL from tide gauges (circles) relative to the 1993–99 mean. (b) The difference in annual mean SLA and RSL for 2007 relative to 2006.

the monthly anomalies for the remainder of 2007 (see, also, Figs. 3.2 and 3.15).

In the Indian Ocean, a negative sea level anomaly occurred off the coasts of Sumatra and Java in September 2006, and a positive anomaly was present just west of this feature. Both high and low patterns grew in amplitude with the low extending northward into the Bay of Bengal and the high extending eastward to the African coast. By January 2007 a high/low pattern in the western/eastern basin resembled the positive mode of the IOD (Saji et al. 1999). The positive anomaly in the western Indian Ocean south of the equator peaked in amplitude during the first half of 2007 and diminished by September 2007. It was followed by a second positive SLA south of the equator that developed in the eastern Indian Ocean during the last quarter of 2007.

Extreme sea level events during 2007, associated with storms and other nontidal variability, are characterized by averaging the 5% highest daily average RSL values relative to the annual mean RSL at each station. The largest extremes generally occur at high-latitude stations due to winter storm activity, with sporadic high values at low-latitude stations (Fig. 3.21a). To determine how anomalous the extremes were at each station during 2007, the percentage of years with extreme values less than 2007 is depicted in Fig. 3.21b. Regions of higher than average extreme sea levels include northern Europe, much of North America, and southern Australia. Regions of lower than average anomalies include the western and central Pacific and the western and central Indian Ocean.

f. The global ocean carbon cycle—C.L. Sabine, R.A. Feely, R. Wanninkhof, and T. Takahashi

1) Air–sea carbon dioxide fluxes

The time and space scales of variability in the air–sea CO_2 flux make it challenging to assess global fluxes based on in situ surface observations. In 1990, Tans et al. (1990) combined 30 yr worth of shipboard pCO_2 observations in an attempt to develop the first global pCO_2 climatology. It excluded much of the Southern Ocean because of lack of data. The first true monthly global climatology was developed in 1997 (Takahashi et al. 1997) using a substantially larger dataset of approximately 250,000 measurements and then updated in 2002 (Takahashi et al. 2002) based on 940,000 measurements. Recently, Takahashi has submitted a revised climatology for publication that combines nearly 3 million measurements collected between 1970 and 2006 (Takahashi et al. 2008). In addition to the substantially larger database of observations, the revised climatology incorporates several other refinements in our understanding of CO_2 variability and fluxes. The annual mean contemporary CO_2 flux over the global oceans is estimated to be a net uptake of 1.4 ± 0.7 Pg-C yr^{-1}. Assuming the preindustrial steady-state ocean was a source of 0.4 ± 0.2 Pg-C yr^{-1} gives a net ocean anthropogenic CO_2 uptake of

1.8 ± 0.7 Pg-C yr^{-1} in 2000 (Takahashi et al. 2007). As with the previous climatologies the estimate is for a non–El Niño year. Since the efflux of CO_2 in the equatorial Pacific is depressed during El Niño periods (Feely et al. 2006), such conditions increase the net CO_2 flux into the ocean. Based on a time series of CO_2 fluxes in the equatorial Pacific (Feely et al. 2006) we estimate that the average CO_2 flux including El Niño years would be about 2.0 ± 0.7 Pg-C yr^{-1}. This value is well within the uncertainty of the ocean CO_2 uptake the estimate provided in Denman et al. (2007) of 2.2 ± 0.5 Pg-C yr^{-1} obtained by independent means.

Figure 3.22 shows a map of annual mean air–sea CO_2 flux climatology. Although the first-order patterns of CO_2 uptake and release have not changed, the revised flux map does vary from previous versions in the details. In general, both the sources and sinks are somewhat stronger in the latest climatology. The observed changes can be attributed not only to the improved database, but also to the revised formulations for calculating flux. Sweeney et al. (2007) have reassessed the bomb ^{14}C inventory and determined it to be about 20% less than the original estimate causing a corresponding 20% decrease in the wind speed dependence of the air–sea gas transfer. Examination of ocean CO_2 time series measurements has shown that, with a few small regional exceptions, global surface water pCO_2 values are increasing at about the same rate as the atmosphere (e.g., Takahashi et al. 2006). To create a climatology with a single nominal year of 2000, data collected prior to 2000 were adjusted to the climatology year by increasing the surface ocean CO_2 values at the same rate as the observed atmospheric CO_2 increase over the time interval. Based on historical pCO_2 observations, two regional exceptions for this adjustment were made in the Bering Sea and the winter high-latitude Southern Ocean. These are areas where vertical mixing is a stronger control on surface pCO_2 values than the atmospheric uptake so no time-dependent adjustment was made (Takahashi et al. 2007). It is important to note that the differences in flux in the different climatologies are not attributed to climate change or decadal variability but rather to improved methodology.

One region where new data has made a noticeable difference in the net flux is in the high-latitude South-

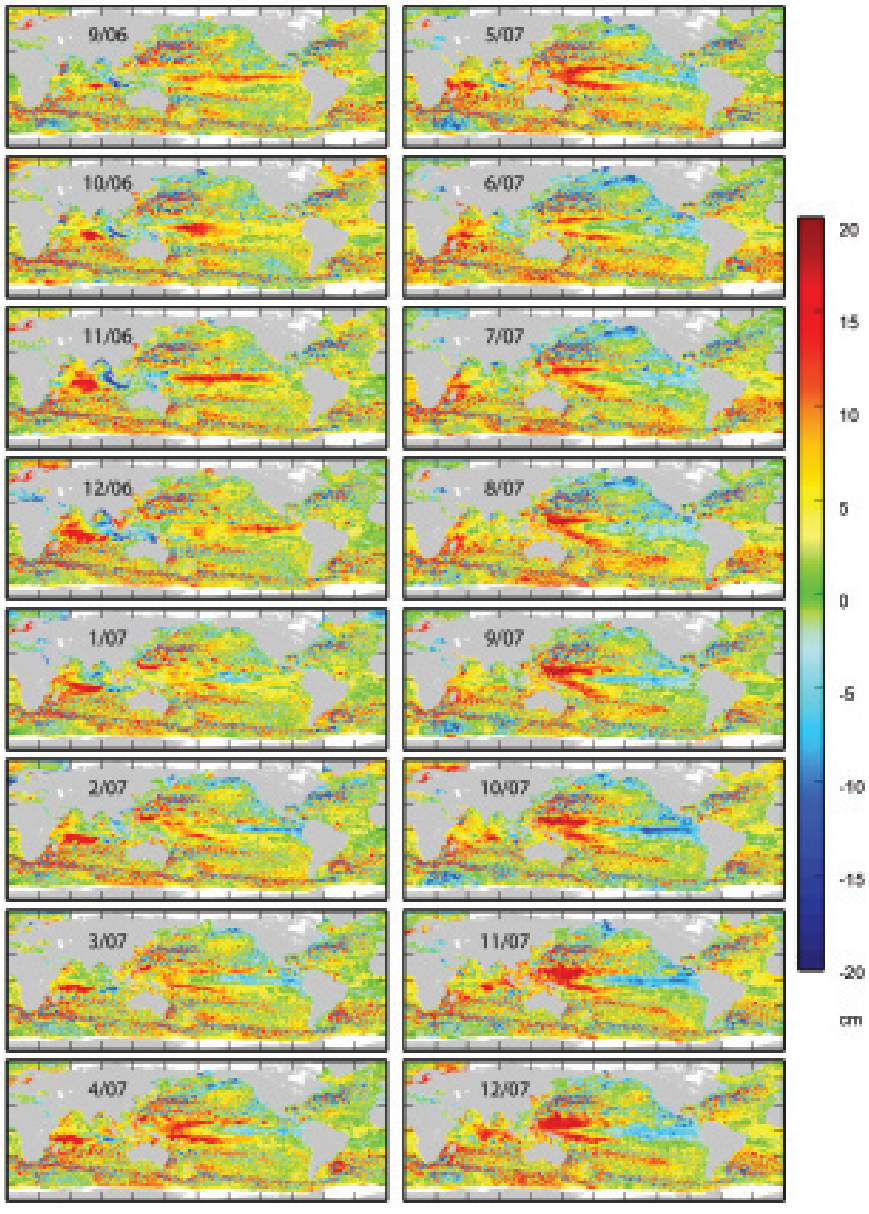

Fig. 3.20. Monthly mean SLA (1993–99 average for each month removed) for Sep 2006 through Dec 2007.

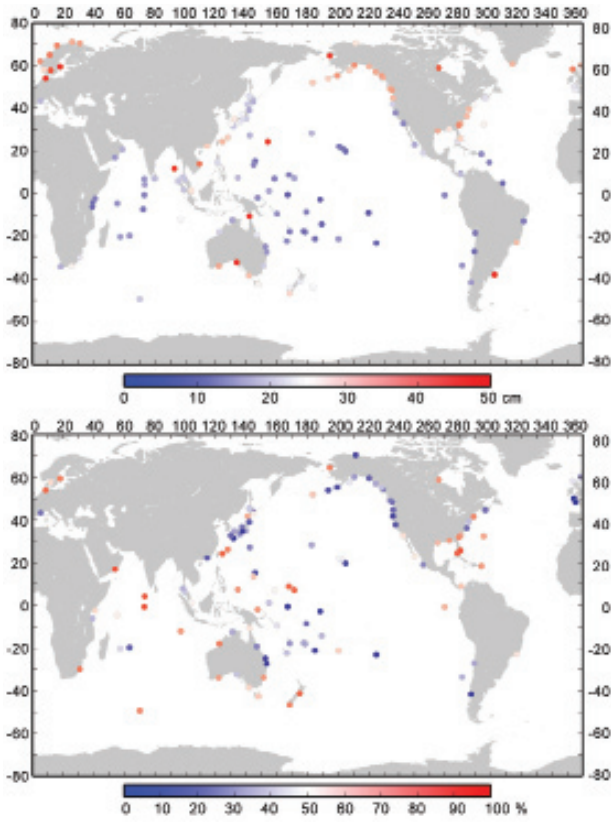

Fig. 3.21. (a) Extreme RSL values during 2007, defined as the average of the 5% largest daily averaged values relative to the annual mean at each station. (b) Percentage of years at each station with extreme RSL values less than in 2007.

ern Ocean between 50° and 62°S where the addition of new data and a new interpolation method utilizing SST significantly reduced the derived net ocean uptake. The lower Southern Ocean uptake is now more consistent with atmospheric inversion estimates of ocean uptake (e.g., Gurney et al. 2004; Jacobson et al. 2007) compared to the previous climatology. Although the new climatology still excludes coastal regions, it does include more regions in the Arctic Ocean where data are becoming available.

Seasonal-to-annual estimates of net air–sea CO_2 fluxes are needed to properly evaluate the changing role of the ocean in the global carbon cycle. The global network of VOS and moored CO_2 systems has grown significantly over the past decade, but interpolation schemes are still needed to develop global flux maps on shorter time frames. We have taken the empirical approach of Lee et al. (1998) and Park et al. (2006) together with global monthly estimates of SST and a high-resolution wind speed assimilation product (available online at http://podaac-www.jpl.nasa.gov/products/product079.html) to develop monthly estimates of global air–sea CO_2 flux between 1995 and 2006. Linear least-squares fits of surface water pCO_2 versus SST are determined for each 4° × 5° pixel of the pCO_2 climatology for three periods: January–April, May–August, and September–December. These relationships are then used together with the interannual SST anomalies to determine pCO_2 anomalies relative to the climatology. Since the climatology specifically excluded data in the equatorial Pacific during El Niño periods, the derived fluxes are only representative of non–El Niño conditions. To better represent the interannual variations in the equatorial Pacific between 5°N and 10°S, CO_2 flux was calculated using surface water pCO_2 formulations of Cosca et al. (2003), including equations for both El Niño and non–El Niño conditions, atmospheric CO_2 from NOAA's Environmental Science and Research Laboratory (GLOBALVIEW-CO2 2007), and the wind speed gas exchange parameterization of Wanninkhof (1992).

The monthly flux map approach was first developed based on the climatology published in 2002, but here we calculate the anomalies relative to the new climatology (Takahashi et al. 2007). Figure 3.23 shows the interannual variability in the net annual air–sea CO_2 flux from 1995 to 2006. The red line shows the flux estimated using the empirical relationships determined by Park et al. (2006) based on the Takahashi et al. (2002) climatology. The blue line uses the same approach as Park et al. but a new set of empirical relationships was derived from the revised climatology. While the overall patterns are similar between the two lines, the revised relationships imply an interannual variability that is about 30% larger than suggested from the original fits. The majority of the interannual variability in the ocean is

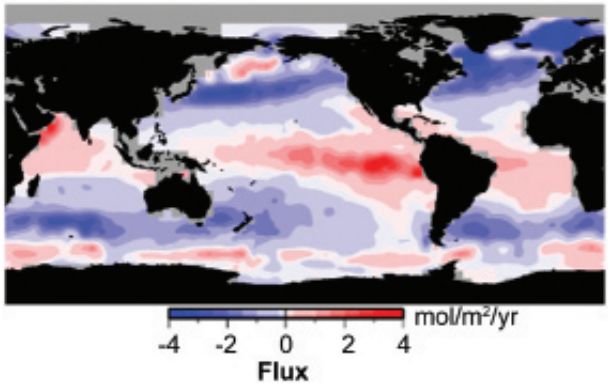

Fig. 3.22. Map of global climatological annual mean CO_2 flux for nominal year 2000 adapted from Takahashi et al. (2007). Negative fluxes represent uptake of CO_2 by the ocean.

typically attributed to ENSO variability in the equatorial Pacific. However, since both formulations use the Cosca et al. (2003) functions in this region, all of the 30% increase in interannual variability comes from the extratropical regions. We attribute this change to improved fits based on more actual observations rather than smoothed interpolated values in the original climatology.

There are significant uncertainties in the seasonal flux map calculations based on several factors, including the assumptions that go into the fits, the quality of the empirical fits, uncertainties in the reanalysis products, and uncertainties in the wind speed relationship for gas exchange. This approach does not account for the biological effects on surface water pCO_2 that are not correlated to temperature. Despite these shortcomings the interannual trends and magnitudes are similar to those obtained from numerical models. These estimates provide a useful observation-based tool for assessing the changing role of the ocean in global climate change. Extension of the global surface ocean CO_2 network will facilitate the development of improved regional algorithms that will lead to more accurate flux maps.

2) Subsurface carbon inventory

In the decade of the 1990s carbon samples were collected and analyzed from approximately 95 research cruises run as part of the international WOCE and the JGOFS. These data were carefully quality controlled and combined into a uniform dataset to make the first global assessment of DIC distributions with sufficient accuracy and coverage to evaluate the distribution of anthropogenic CO_2 in the ocean (Sabine et al. 2004; Key et al. 2004). Sabine et al. (2004) estimated that the total inventory of anthropogenic CO_2 in the ocean in the year 1994 was 118 ± 19 Pg C, accounting for 48% of the CO_2 released from fossil fuel burning between 1800 and 1994. This one-time global survey, however, could not provide information on how ocean carbon inventories have evolved over time or how the storage has varied geographically over different time periods.

In 2003, the United States CLIVAR/CO_2 Repeat Hydrography Program began reoccupying a subset of the WOCE/JGOFS lines in an effort to evaluate the decadal changes in ocean carbon inventories. The program has identified 19 hydrographic sections distributed around the global ocean that will be reoccupied approximately every 10 yr. This work is being conducted in collaboration with other nations that have similar repeat hydrography programs. In 2007 the U.S. CLIVAR/CO_2 Repeat Hydrography Program completed a meridional section nominally along 90°E in the Indian Ocean marking the half-way point of the U.S. portion of the decadal survey effort (Fig. 3.24).

Isolating the anthropogenic component of the DIC change is not simply a matter of subtracting the values measured on two cruises separated in time. Aliasing from mesoscale eddies and frontal oscillations that displace isopycnal surfaces (Haine and Gray 2001; Peacock et al. 2005) as well as variations in water mass properties associated with climate modes such as the ENSO (Feely et al. 2002, 2006) can complicate the signal when comparing two cruises separated in time. To correct for these variations, we use the multiple linear regression approach first introduced by Wallace (1995). The application of these corrections varies depending on data quality and the oceanographic conditions along the section, thus each section must be evaluated separately. A full global assessment of ocean DIC changes cannot be made until the resurvey of the oceans is completed in the next few years. However, each updated ocean section provides incremental insight into how carbon uptake rates are evolving spatially and temporally.

Table 3.1 summarizes the current best estimates of anthropogenic CO_2 accumulation along representative north–south cruise tracks in the Atlantic and Pacific

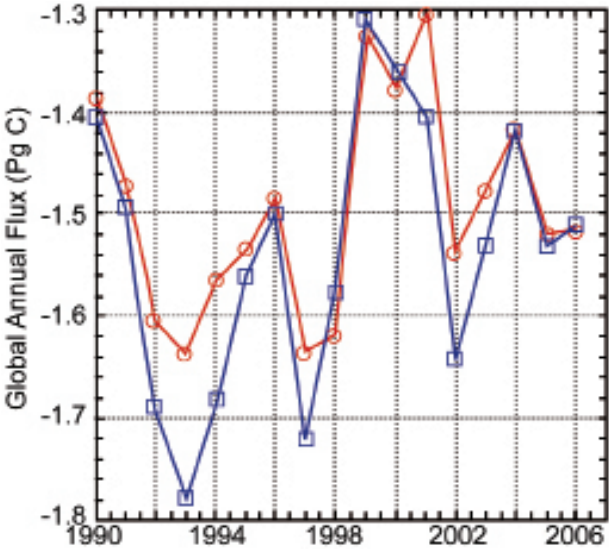

Fig. 3.23. Plots of global annual ocean CO_2 uptake using empirical functions described in the text. Red line is based on functions derived from Takahashi et al. (2002). Blue line is based on functions derived from Takahashi et al. (2007). The difference between the two lines gives a sense of the uncertainty in the estimates and how the improved data coverage in the 2007 climatology impacts the estimated interannual variability.

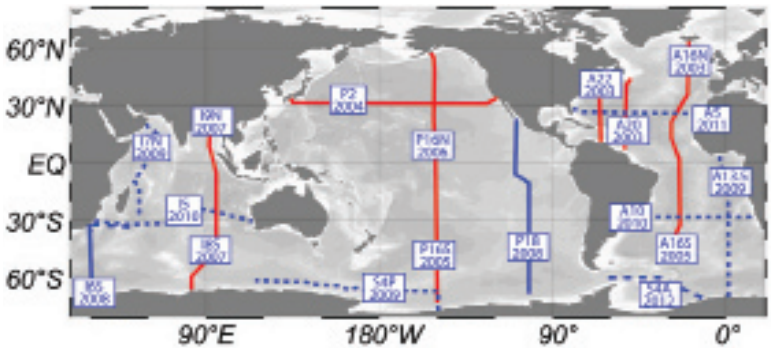

Fig. 3.24. Map of proposed and completed cruises for the U.S. CLIVAR/CO_2 Repeat Hydrography Program. Red lines show completed cruise, blue solid lines are 2008 cruises and the blue dashed lines show proposed cruises to complete the global survey.

Oceans over the last decade. The North Atlantic shows the largest increase, consistent with the long-term accumulation of Sabine et al. (2004), illustrating the importance of North Atlantic Deep Water formation as a mechanism for transporting anthropogenic CO_2 into the ocean interior. The formation of mode and intermediate waters in the Southern Hemisphere also contributes to the substantial DIC increases in the South Atlantic and South Pacific. The North Pacific shows a relatively modest increase because of the lack of deep-water formation and restricted intermediate water formation in that region.

Figure 3.25a shows the preliminary estimates of the accumulation of anthropogenic CO_2 in the Indian Ocean between the 1995 WOCE/JGOFS cruises and the 2007 repeat hydrography cruise. To a first order, the pattern of accumulation looks very similar to the anthropogenic CO_2 changes estimated by Sabine et al. (1999) between the 1978 GEOSECS cruise along 90°E and the 1995 WOCE/JGOFS cruise (Fig. 3.25b). Both sections show very little penetration of anthropogenic CO_2 into the high-latitude Southern Ocean with the deepest penetration, approximately 1,200–1,300 m, associated with the subtropical convergence zone at about 40°S. There is a suggestion of slightly deeper penetration of the 5 μmol kg^{-1} (minimum detection limit) contour and larger total inventory changes in the decade after WOCE/JGOFS compared to the decade before WOCE/JGOFS, but a full assessment of the uncertainties and patterns in these estimates is still underway.

These latest results show conclusively that anthropogenic CO_2 is continuing to accumulate in the Atlantic, Pacific, and Indian Oceans. Thus far, they agree with the long-term storage patterns of Sabine et al. (2004) that the largest inventories are associated with the regions where water masses are being formed and moving into the ocean interior. However, a single transect through an ocean basin is not sufficient for characterizing the full patterns of anthropogenic CO_2 storage. Results in both the Pacific and Atlantic Oceans have shown that circulation changes can have a significant impact on the net total change in carbon inventory on decadal time scales. In some cases these changes may enhance the storage of carbon and in other cases they may decrease the uptake resulting from rising atmospheric CO_2. Because circulation and biological changes can vary in cycles, it is critical to continue to monitor the changes in carbon inventories and how they interact with the secular increases in anthropogenic CO_2. As additional cruises are completed the full picture of the decadal storage will be developed.

g. Global ocean phytoplankton and productivity—M.J. Behrenfeld, D. A. Siegel, and R. T. O'Malley

Phytoplankton, the single-celled photosynthetic prokaryotic and eukaryotic organisms of the upper sunlit "photic" zone, are the base of ocean ecosystems and the primary conduit through which inorganic carbon is transferred into the organic carbon pool, driving the biological pump. This photosynthetic uptake of CO_2 by phytoplankton represents a key mechanism

Table 3.1. Estimates of ocean column inventory changes in anthropogenic carbon (mol C m^{-2} yr^{-1}) over the last decade.

	Atlantic Ocean (along 25°W)	Pacific Ocean (along 152°W)	Indian Ocean (along 90°E)
Northern Hemsphere	0.63	0.25	*
Southern Hemisphere	0.75	0.41	*

*Indian Ocean changes are still being evaluated.

through which ocean biology influences climate. Climate, in turn, plays a key role in regulating the growth and biomass of phytoplankton by controlling the distribution of nutrients and the availability of light during the growing season. The interaction between climate and phytoplankton is complex. The net effect of a shift in regional climate can be either an increase or decrease in phytoplankton abundance and productivity depending on how that climate shift impacts limiting resources (light, nutrients) for phytoplankton in the region. Nevertheless, in the broadest sense, ocean circulation–ecosystem models predict that future climate warming will result in a net reduction in mixed layer phytoplankton biomass and productivity in low-latitude, permanently stratified oceans due to an intensification in nutrient stress, while yielding a net increase at higher latitudes due largely to an increase in growing season and mixed layer light levels (via enhanced stratification) (Boyd and Doney 2002; Bopp et al. 2001; Le Quéré et al. 2003; Sarmiento et al. 2004).

Satellite observations of ocean color provide the best means for assessing interannual variability in phytoplankton abundance and productivity on a global basis. The only two U.S. sensors to provide global climate-quality ocean color data are the SeaWiFS (1997 to end of 2007) and the subsequent Aqua MODIS (2002 to present). Thus, 2007 was a milestone year marking the first full decade of climate-quality ocean color data. One of the primary products derived from satellite ocean color is surface-layer Chl_{sat}. Chlorophyll is not a robust measure of phytoplankton biomass, as it is strongly influenced by mixed layer growth conditions (light and nutrients), but it does provide an integrated index of phytoplankton abundance and physiology (Behrenfeld et al. 2005; Siegel et al. 2005a). ΣChl, a more relevant property for ocean biology and biogeochemistry, is roughly proportional to the square root of Chl_{sat} and can be reliably estimated using any one of a wide range of published expressions (e.g., Morel and Berthon 1989). From ΣChl, NPP can be derived provided additional information on incident light levels, attenuation coefficients, and physiology is available (Behrenfeld and Falkowski 1997; Carr et al. 2006).

Surface chlorophyll concentrations vary globally by three orders of magnitude (roughly 0.03 to >30 mg m^{-3}), with a first-order spatial distribution reflecting variations in light, nutrients, and grazing pressure (Fig. 3.27a). Global average Chl_{sat} for the 10-yr SeaWiFS record has a mean value of 0.342 mg m^{-3}, but exhibits strong seasonal cycles that peak during boreal summer at 0.381 mg m^{-3} (range: 0.360–0.400 mg m^{-3}) and are minimal in austral summer at 0.302 mg m^{-3} (range: 0.285–0.320 mg m^{-3}). This seasonal cycle largely reflects hemispheric differences in high-latitude summer blooms, with Southern Hemisphere blooms above 45° latitude generally diminished relative to the Northern Hemisphere due to the prevalence of iron-limiting conditions in the Southern Ocean. For 2007, global average Chl_{sat} was 0.349 mg m^{-3} (close to the climatological mean), with monthly values ranging from 0.297 to 0.400 mg m^{-3} (Fig. 3.27a).

Global photic zone chlorophyll varies by only 1.3 orders of magnitude, but exhibits a similar spatial distribution as Chl_{sat} (Fig. 3.27b). The global mean ΣChl value for 2007 was 14.2 mg m^{-2}, which is identical to the climatological mean for the SeaWiFS record. The spatial distribution of ΣChl during 2007 nevertheless exhibited some interesting deviations from the climatological pattern (Fig. 3.27c). In 2007,

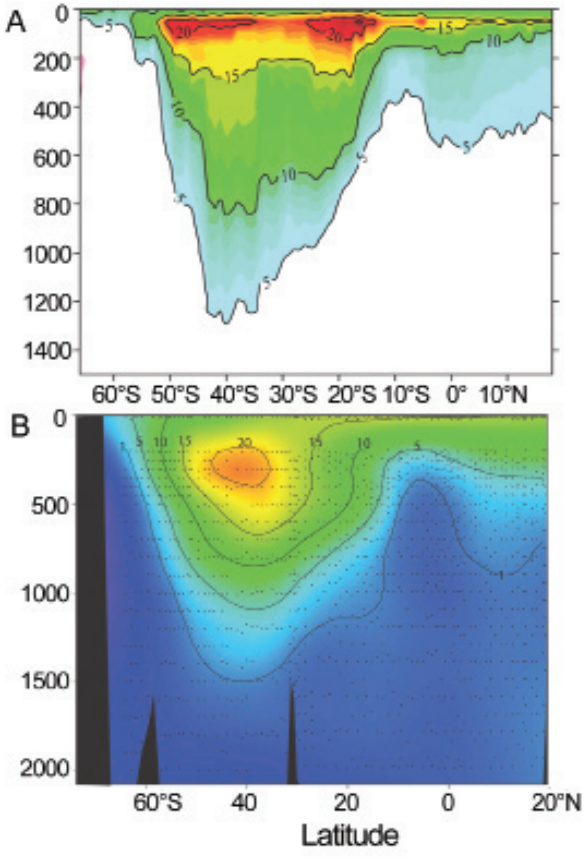

Fig. 3.25. Sections of change in anthropogenic CO_2 (μmol kg^{-1}) based on observations made in the Indian Ocean and Southern Ocean (along ~90°E) for the time period (a) 2007–1995 and (b) 1995–78. The black dots in (b) indicate the measurement locations used for the calculations.

Since the beginning of the industrial revolution the release of CO_2 from humankind's collective industrial and agricultural activities has resulted in atmospheric CO_2 concentrations that have risen from preindustrial levels of about 280 ppmv to nearly 385 ppmv. The atmospheric concentration of CO_2 is now higher than experienced on Earth for at least the last 800,000 yr and probably over 20 million yr, and is expected to continue to rise at an increasing rate. The oceans have absorbed approximately 525 billion tons of carbon dioxide from the atmosphere, or about one-third of the anthropogenic carbon emissions released. This absorption has proven beneficial in damping the rise of carbon dioxide concentrations in the atmosphere; however, the ocean's uptake of carbon dioxide is having negative impacts on the chemistry and biology of the oceans. Hydrographic surveys and modeling studies have revealed that the chemical changes in seawater resulting from the absorption of carbon dioxide are lowering seawater pH. For example, the time series data at Ocean Station Aloha shows an average pH decrease of approximate 0.02 units per decade in the northeast Pacific (Fig. 3.26; after Feely et al. 2008). The pH of ocean surface waters has already decreased by about 0.1 units from an average of about 8.21 to 8.10 since the beginning of the industrial revolution (Feely et al. 2004). Estimates of future atmospheric and oceanic carbon dioxide concentrations, based on the IPCC CO_2 emission scenarios and coupled ocean–atmosphere models, suggest that by the middle of this century atmospheric carbon dioxide levels could reach more than 500 ppm, and near the end of the century they could be over 800 ppm. This would result in an additional surface water pH decrease of approximately 0.3 pH units by 2100 (Feely et al. 2004; Orr et al. 2005). When CO_2 reacts with seawater, the reduction in seawater pH also reduces the availability of carbonate ions, which play an important role in shell formation for a number of marine organisms such as corals, marine plankton, and shellfish. This phenomenon, which is commonly called "ocean acidification," could have profound impacts on some of the most fundamental biological and geochemical processes of the sea in coming decades. Some of the smaller calcifying organisms are important food sources for higher marine organisms. Declining coral reefs, which are presumed to be due to increases in temperature and decreases in carbonate ion, have been observed in the oceans (Hoegh-Guldberg et al. 2007; Cooper et al. 2008). Further decline of the coral reefs would have negative impacts on tourism and fisheries. Abundance of commercially important shellfish species may also decline and negative impacts on finfish may occur. This rapidly emerging scientific issue and possible ecological impacts have raised serious concerns across the scientific and fisheries resource management communities.

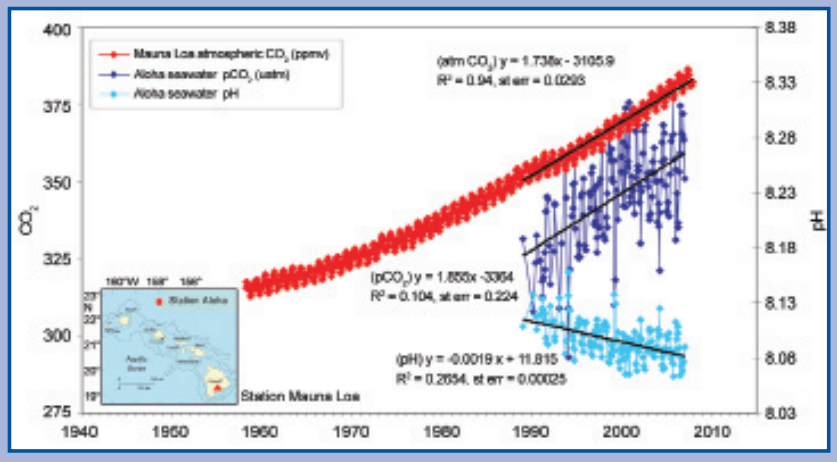

FIG. 3.26. Time series of atmospheric CO_2 at Mauna Loa (ppmv) and surface ocean pH and pCO_2 (µatm) at Ocean Station Aloha in the subtropical North Pacific Ocean. Note that the increase in oceanic CO_2 over the last 17 yr is consistent with the atmospheric increase within the statistical limits of the measurements. [Mauna Loa data: Dr. Pieter Tans, NOAA/ESRL, www.esrl.noaa.gov/gmd/ccgg/trends; HOTS/Aloha data: Dr. David Karl, University of Hawaii, http://hahana.soest.hawaii.edu.]

values of ΣChl were 10% or more above climatological average values in 11% of the global ocean area and 10% or more below climatological values in 13% of the ocean, with 46% of the gains and 58% of the losses occurring in the permanently stratified oceans (approximated by waters with annual average SST > 15°C). The patterns observed here are consistent with the recent satellite data analyses of Polovina et al. (2008).

Zonal average anomalies in ΣChl for 2007 relative to climatological values were inversely related to changes in SST equatorward of 45° latitude (Fig. 3.28). While this result at first appears consistent with earlier model expectations of decreased biological productivity from enhanced nutrient stress in the tropics and subtropics under warming conditions, Behrenfeld et al. (2008) show that physiological responses to changing mixed layer light conditions

(i.e., "photoacclimation") also play an important role. In contrast to the stratified oceans, a simple relationship between ΣChl and temperature changes at latitudes poleward of 45° is not observed in the annual zonal anomalies for 2007 (Fig. 3.28).

Global SST and chlorophyll values for 2007 were very close to climatological average values for the SeaWiFS period, making a relationship between these two properties difficult to decipher. A much clearer view of the ocean biology–climate link emerges when the 2007 data are viewed in the context of the entire 10-yr record (Fig. 3.29). Monthly anomalies in ΣChl for Northern Hemisphere high-latitude regions with annual average SST <15°C (roughly >45°N) exhibit an overall increase ($p < 0.001$) between 1997 and 2007, with a secondary oscillation peaking first in 2000–01 and again in 2006–07 (Fig. 3.29a). These changes in ΣChl exhibited a striking inverse correspondence with anomalies in SST (Fig. 3.29a). In the permanently stratified lower-latitude oceans, chlorophyll anomalies rose rapidly during the 1997 to 1999 El Niño–La Niña transition and then generally decreased thereafter (Fig. 3.29b). These chlorophyll changes also exhibit a strong inverse correlation with low-latitude SST anomalies (Fig. 3.29b). Finally, ΣChl anomalies at high southern latitudes indicate a slight but significant ($p < 0.001$) rise over the 1997 to 2007 period, which once again is inversely correlated with SST changes (Fig. 3.29c). In summary, all three zones show clear relationships between chlorophyll and climate fluctuations, but in each case either the sign of the relationship or the underlying physiology is inconsistent with model predictions.

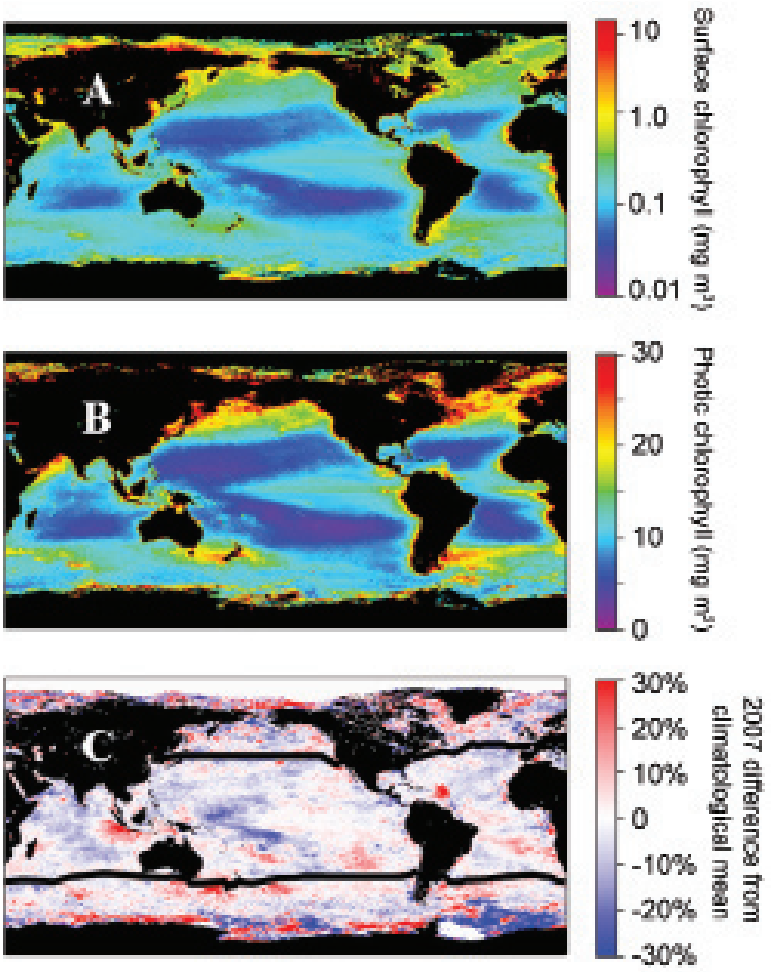

Fig. 3.27. (a) Average surface Chl_{sat} for 2007. (b) Average ΣChl for 2007. (c) Percentage difference between 2007 annual average ΣChl and climatological mean values for the SeaWiFS record. Heavy black lines demark low-latitude permanently stratified oceans (annual average SST >15°C) from higher-latitude regions (annual average SST <15°C).

The 2007 values and 10-yr chlorophyll record described above are based on the OC4v4 chlorophyll algorithm, the operational algorithm for SeaWiFS. The drawback of an empirical wavelength ratio algorithm, such as OC4v4, is its limited capacity to account for independent behavior in the multiple optically active in water constituents regulating the ocean color signal (IOCCG IOP report 2006). To assess the role of independent variations in ocean optical properties on our above results, we repeated the analysis using chlorophyll estimates from the alternative GSM semianalytical algorithm (Maritorena et al. 2002). The GSM inverts ocean color data to simultaneously solve for the independent contributions of chlorophyll absorption, particulate backscattering, and absorption by cDOM. The GSM algorithm yields monthly average chlorophyll values for the stratified oceans that are highly correlated with OC4v4 estimates ($r^2 = 0.84$), but are on average 34% lower. For the higher-latitude regions, GSM monthly Chl_{sat} values are more divergent from ($r^2 = 0.22$) and 43% lower than the OC4v4 estimates. These differences are due to the variable fraction of light absorption attributed to cDOM in GSM (Siegel et al. 2005b). For 2007, the GSM yields a global average Chl_{sat} of 0.216 mg m^{-3}, which is 38% lower than the global OC4v4 estimate above. When applied to

a simple NPP algorithm (Behrenfeld and Falkowski 1997), the GSM and OC4v4 chlorophyll values for 2007 yield productivity estimates of 46.6 and 55.1 Pg C yr^{-1}, respectively. However, although the two algorithms diverge significantly in chlorophyll and NPP estimates, their monthly anomalies in ΣChl for the full SeaWiFS record are in close agreement, indicating that the ocean biology–climate relationship illustrated in Fig. 3.29 is largely insensitive to choice of chlorophyll algorithm.

An added benefit of the semianalytical approach is that it provides estimates of particulate backscatter coefficients, which can be used to assess phytoplankton carbon biomass (Behrenfeld et al. 2005; Westberry et al. 2008). Behrenfeld et al. (2008) used this additional phytoplankton biomass information to resolve the underlying basis for interannual changes in Chl_{sat} observed over the SeaWiFS record. They found that changes in Chl_{sat} between September 1997 and December 2000 were largely due to changes in phytoplankton abundance. After 2000, however, phytoplankton biomass was relatively invariant and trends in Chl_{sat} were largely due to physiological changes in intracellular pigmentation. Between 2001 and 2006, these physiological adjustments could be primarily attributed to changes in global mixed layer light levels, but from 2006 through 2007 changes

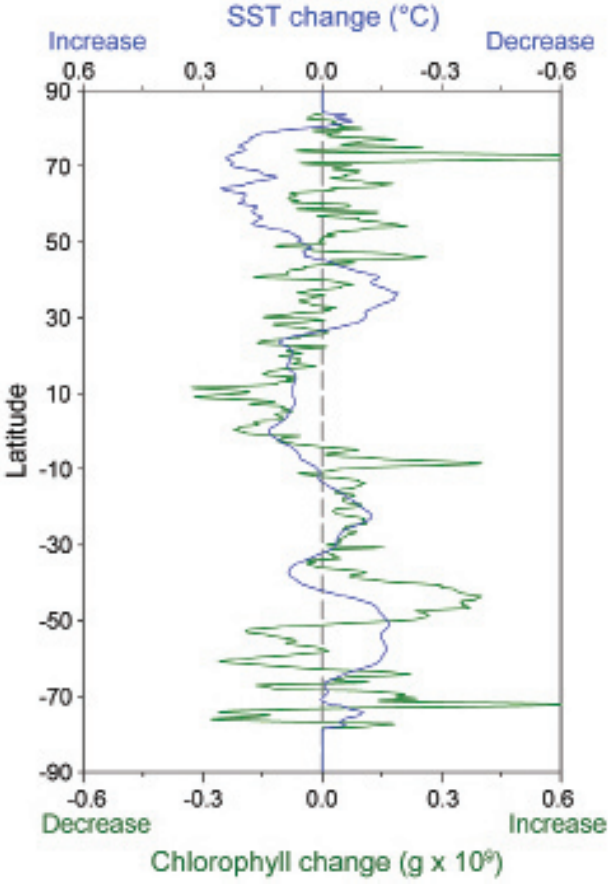

Fig. 3.28. Changes in ΣChl (green line, bottom axis) and SST (blue line, top axis) calculated as the difference between 2007 and climatological average values for the SeaWiFS period. Note that ΣChl changes show decreases on the left and increases on the right (bottom axis), while SST changes show increases on the left and decrease on the right (top axis). SST changes were calculated using only pixels where chlorophyll data were available.

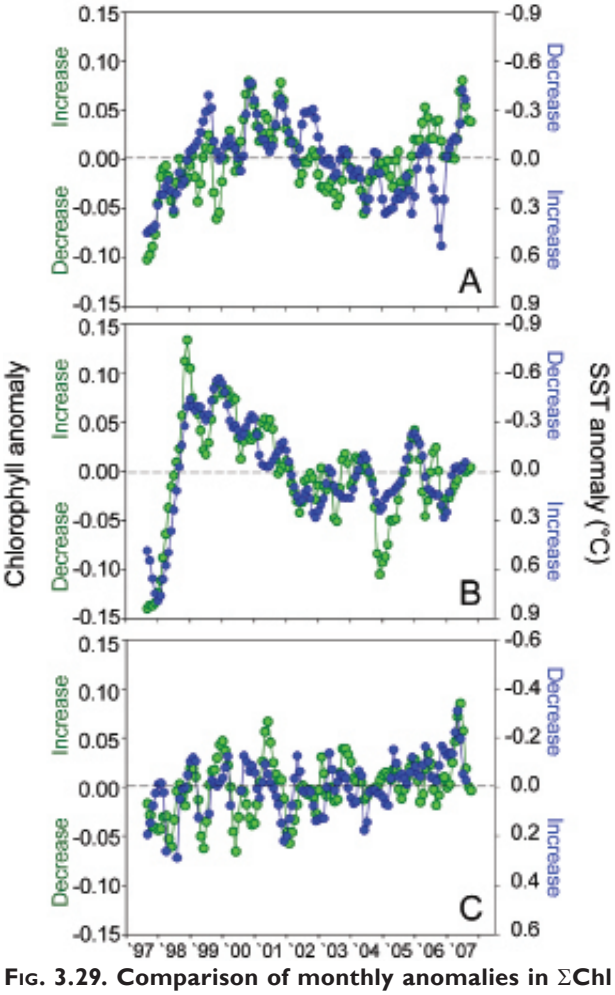

Fig. 3.29. Comparison of monthly anomalies in ΣChl (green symbols, left axis) and SST (blue symbols, right axis) for the 10-yr SeaWiFS record. (a) Northern waters with annual average SST <15°C. (b) Permanently stratified waters with annual average SST >15°C. (c) Southern waters with annual average SST <15°C. Horizontal dashed line indicates monthly climatological average values. Note, left axes increase from bottom to top, while right axes decrease from bottom to top. Also note that all left axes have the same range, while the right axis in (c) has a smaller range than in (a) and (b).

in global mixed layer nutrient levels appeared to be more important. Thus, although global Chl_{sat} values for 2007 are close to the climatological average for the SeaWiFS era, their ecological basis (i.e., combined influence of biomass and physiology) appears dissimilar from all years prior to 2006 (Behrenfeld et al. 2008).

A decade of global observations has demonstrated an exceptionally close pole-to-pole link between phytoplankton chlorophyll variability and coincident fluctuations in climate, with warming trends associated with decreases in chlorophyll and cooling trends associated with increases. Unfortunately, absence of plans to replace the aging MODIS and now dysfunctional SeaWiFS sensors, which are the only sources of climate-quality ocean color data records, jeopardizes further elucidation of this remarkable relationship between climate and ocean biology, observations of which contrast sharply with relationships predicted from ocean circulation–ecosystem models.